

Femtosecond spectroscopy studies of recombinant hemoglobin I
of the clam *Lucina pectinata* (*Gmelin, 1791*)

By
Cacimar A. Ramos Álvarez

A dissertation submitted in partial fulfillment of the requirements for the degree of

DOCTOR OF PHILOSOPHY
in
Applied Chemistry
(Biophysics)

University of Puerto Rico
Mayagüez Campus
2011

Approved by:

Juan López Garriga, Ph. D.
President, Graduate Committee

Date

Miguel E. Castro, Ph. D.
Member, Graduate Committee

Date

Samuel Hernández, Ph. D.
Member, Graduate Committee

Date

Gustavo López, Ph. D.
Member, Graduate Committee

Date

Nilda E. Aponte, Ph. D.
Representative on Graduate Studies

Date

Francis Patron, Ph. D.
Chairperson, Chemistry Department

Date

ABSTRACT

Lucina pectinata (Gmelin, 1791) is a clam that can be found in sulfide-rich muds in the coastal mangroves of the southwest coast of Puerto Rico. It contains three different hemoglobins in the gill tissue, hemoglobin I, II and III (HbI, HbII and HbIII, respectively), each one characterized by distinct physical-chemical properties. Hemoglobin I (HbI) is a monomeric protein of 142 amino acid residues, and it is responsible for oxygen and/or hydrogen sulfide transportation. These proteins present an excellent scenario for the study of dynamics of their reaction with diatomic small molecules and H₂S. With the development of a state-of-the-art ultrafast laser system and experimental setup we were able to study the initial steps in the reaction of HbI and HbI mutants in various electronic states with its native ligand (H₂S) in the fs to ps time regime. The HbI-H₂S kinetics showed a second component of ~12ps, two times faster than the same component for the metaquo specie. Furthermore the transient absorption spectra do not show the classical ligated to unligated trace indicating the presence of at least three different species during the initial photolysis steps. It has been observed that in the presence of H₂S HbI can undergo reduction from its Fe^{III} state, the mechanism is still unknown but our experiments demonstrate that this could be feasible. Measurements taken for the rHbI ferrous complex, demonstrated that small fraction of photo-oxidation of the sample occurred.

Resumen

La almeja *Lucina pectinata* (Gmelin 1791) es un organismo que se encuentra en el área de los lodazales del mangle en la costa suroeste de la isla de Puerto Rico. Esta almeja contiene en su tejido tres hemoglobinas, la hemoglobina I, II y III. Cada una de ellas posee propiedades químico-físicas características con funciones diferentes. La primera de esas hemoglobinas, Hbl, es una proteína monomérica que consta de 142 residuos de aminoácidos y se cree es la responsable del transporte de oxígeno y/o ácido sulfídrico (H_2S). Esta, y las otras hemoglobinas presentes, proveen un excelente escenario para el estudio de la dinámica de reacción con moléculas diatómicas gaseosas, como por ejemplo H_2S . Además de que para el caso de Hbl, ese es su ligando natural. Para ello se desarrolló e implementó un sistema de láseres ultra rápido para medir los pasos iniciales de la interacción de la hemoglobina con el ligando H_2S . Las curvas cinéticas de Hbl- H_2S muestran un segundo componente de ~12 ps, dos veces más rápido que el obtenido para la especie metaquo. Al examinar las curvas de absorción de las especies transitorias vemos que el complejo no exhibe un comportamiento clásico de especie enlazada a especie no enlazada. Al parecer y basados en estos datos podemos decir que debe haber al menos tres especies involucradas en la foto-excitación del complejo Hbl- H_2S . Se encontró que se genera una especie excitada en alrededor de 3.4 ps y que la recombinación geminal del H_2S ocurre alrededor de 12 ps.

To my grandmother Julia and
My son Eieri

ACKNOWLEDGEMENTS

I would like to express my gratitude; first to my chairman and friend PhD. Juan López Garriga for all these years of knowledge and learning; for giving me the opportunity of doing all those things that many consider impossible. I would like to thank my graduate committee for accepting to participate in this endeavor and for their teaching and lectures during all of these years. My gratitude to the people from the Laboratory of Optics and Biosciences (LOB) at the Ecole Politechnique at Paris France for allowing me to conduct part of my experiments in their facilities. Thanks to the Science on Wheels Educational Center for their financial support and for giving me the joy of teaching students the “magic” and “fun” of science.

Table of Contents

Abstract	ii
Resumen	iii
Acknowledgements	v
Table of Contents	vi
List of Tables	ix
List of Figures	x
List of Abbreviations	xiv
1 Introduction	1
1.1 Specific Goals	8
1.1.1. Goal 1. Optimize the mutant expression protocol to generate higher quantities of recombinant protein	8
1.1.2. Goal 2. To incorporate a 3D detection system and a fast data acquisition system.	8
1.1.3. Goal 3. To create the software tools needed to merge the detection with the time resolution of the experiments.	9
1.1.4. Goal 4. To incorporate a double beam setup for data acquisition.	10
1.1.5. Goal 5. To develop and construct a suitable sample handling mechanism.	10
1.1.6. Goal 6. To incorporate global fitting techniques for data handling and reduction.	10
1.1.7. Goal 7. To determine the dynamics description of the recombinant Hbl from <i>Lucina pectinata</i> toward the interaction with H ₂ S.	11
2 Material an Methods	12

2.1.	<u>Wild type (wt)- Hbl and Hbl mutants preparation</u>	12
2.2	<i>Optimization of the fermentation protocol:</i>	14
2.3.	Protein extraction and purification.	18
2.4.	Complex formation.	18
2.5.	Instrumentation and data acquisition.	21
	2.5.1. RUM UltrasFast laser spectroscopy setup.	21
	2.5.2. Sampler Cell Holder and mechanism.	23
	2.5.3. Ecole Politechnique ultras fast spectroscopy setup.	24
2.6.	Data acquisition.	24
2.7.	Software for data acquisition.	25
2.8.	Data handling and mathematical fitting.	26
3	Results	
	3.1 Results for Goal 1	28
	3.2. Results for Goal 2	36
	3.3. Results for Goals 3, 4 and 5	43
	3.4. Results for Goal 6	50
	3.5. Results forGoal 7	55
	3.5.1. Ferrous sample (Fe^{II})	58
	3.5.2. Ferric Wt Hbl (Fe^{III})	61
	3.5.3. Ferric Wt Hbl (Fe^{III})	64
	3.5.4. $\text{Fe}^{\text{II}} \text{NO}$ (Fe^{II})	67
4	Discussion	69
4.1.	Ferrous rHbl sample (Fe^{II})	69
4.2.	Ferric rHbl sample (Fe^{III})	73

4.3.	Ferric H ₂ S-rHbl sample (Fe ^{III} -H ₂ S)	77
5	Conclusions	89
6.	References	90
7.	Appendix	94

List of Tables

Table		Page
Table 3.1.	Summarized comparison between the old fermentation method and the newly developed method.	29
Table 3.2.	Wet pellet yield of the various fermentation process utilizing the old and the new method	34
Table 3.3.	Kinetic Fit values for the different complexes	57
Table 3.4.	Singular Values for the SVD analysis of the ferrous rHbI data.	60
Table 3.5.	Singular Values for the SVD analysis of the ferrous rHbI data	63
Table 3.6.	Singular Values for the SVD analysis of the ferrous rHbI data	66

List of Figure

Figure		Page
Figure 1.1.	Hbl reactive center, showing the residues around the distal and proximal position.	3
Figure 2.1	<i>Lucina pectinata</i> shells after the ctenidia was removed for protein extraction. The clams were collected on the mangrove in the southwest coast of Puerto Rico.	14
Figure 2.2	Fast performance liquid chromatography (FPLC) equipment used for the separation and purification of the different hemoglobins.	13
Figure 2.3.	Pre-fermentation growth steps, for inoculation of the fermentor.	17
Figure 2.4.	Fermentation system for bacterial growth and protein expression showing the control unit the vessel, and the connections.	17
Figure 2.5.	Homemade tonometer system for sample degasification and complex-preparation. The system included a vacuum pump a manifold, several control valves, and a pressure/vacuum gauge.	21
Figure 2.6.	UV-Vis soret region spectra for rHbl complexes,(Orange-Deoxy sample, Purple- Metaquo sample and Red-H ₂ S complex).	21
Figure 2.7.	Femtosecond laser system: laser table and experimental setup.	23
Figure 2.8.	Experimental optical setup: sample and detection area.	23
Figure 3.1.	Bioflo 110 fermentor control unit screen showing the various parameters that can be monitored and changed.	29
Figure 3.2.	Growth curve for the experiment in which Mg ⁺² were added halfway through the experiment. The first section indicates a lag phase at ~OD=10; in the second section, the stationary phase OD=50 after the addition of Mg ⁺² .	31

Figure 3.3.	Bacterial growth curve for the recombinant Hbl species. The black trace indicates the old method and the red trace the new improved method.	31
Figure 3.4.	Growing curves for various mutants using the improved fermentation protocol. Black squares→recombinant HBI, red circles→ValB10 Mutant, Blue triangles→ValE11 and green triangles→HisE7.	33
Figure 3.5.	Intensifier couple device coupled to the monochromator for wavelength range acquisition.	36
Figure 3.6.	Software central core algorithm flow chart.	36
Figure 3.7	Software user interface windows: area I -file name and directory, area II -Delay line parameters, area III -detector parameters, area IV -plot area, area V -Multi and random track settings, area VI -slice and transient specific transient absorption spectra plot, and area VII -notices window	39
Figure 3.8.	Designed cell holder; view of the moving mechanism.	43
Figure 3.9.	Front view of the cell holder mechanism and the sample cell. Notice how half of the cell looks filled with sample and the other part is empty.	43
Figure 3.10.	Double probe beam array sketch.	45
Figure 3.11.	Picture of the modified laser table to accommodate a double beam array. The beam splitter and mirror mounting were home built.	45
Figure 3.12.	ICCD chip image showing two separate areas illuminated by the signal and the background beam	47
Figure 3.13.	Software graph window view while acquiring data with the two beam setup. It has two random tracks and each track is 127 pixels high	47
Figure 3.14.	User interface of the virtual instrument created in Labview for data SVD data analysis. The input of the software is the text file with	50

the intensity matrix, and the output will be three files with each deconvoluted matrix		
Figure 3.15.	Graphic programming of the SVD analysis VI tool.	50
Figure 3.16.	Intensity matrix.	51
Figure 3.17.	Screen shot of the developed program running with rHb sample for testing stability. Notice that only 50 accumulation where taken per scan.	55
Figure 3.18.	Absorption spectra of two consecutive delay positions without pump (red and black). On Blue the difference between the two.	55
Figure 3.19.	Kinetic traces of the first SVD component of for the various mutants with the different oxidation states.	56
Figure 3.20.	Difference transient absorptions at various delay positions (4-10ps) of the ferrous (Fe^{II}) rHbl sample.	58
Figure 3.21.	Difference transient absorptions at various delay positions (4-47ps) of the ferrous (Fe^{II}) rHbl sample.	58
Figure 3.22.	First 3 SVD transient absorption components for the ferrous (Fe^{II}) rHbl sample each multiplied by their respective singular values.	59
Figure 3.23.	Difference transient spectra of the ferric rHbl sample at various delay positions.	61
Figure 3.24.	Difference transient spectra of the ferric rHbl sample at various delay position.	61
Figure 3.25.	First 4 SVD components of the ferric (Fe^{III}) sample multiply by its respective singular value.	62
Figure 3.26.	Transient spectra of the ferric- H_2S rHbl sample at short time scale.	64
Figure 3.27.	Transient spectra of the ferric- H_2S rHbl sample at long time scale.	64
Figure 3.28.	First three SVD components for the Ferric- H_2S rHbl sample multiply with their respective singular value.	65
Figure 3.29.	Transient absorption of rHbl- Fe^{II} NO reduce with ascorbate at different delay positions.	67

Figure 3.30.	First three SVD components for the rHbI-Fe ^{II} NO sample. Each trace was multiply by their respective singular value.	67
Figure 4.1.	Comparison between the first SVD component for the ferrous rHb(Fe ^{II}) sample with the steady state spectrum of the same sample.	70
Figure 4.2..	Normalize data of the ferrous (Fe ^{II}) rHbI sample to show the blue shift of the induce absorption signal (4ps is the flat black line). The insert show the isobestic region for the same plot.	70
Figure 4.3	Panel A show the first 2 SVD components for the Ferrous rHbI sample. The dotted red line is the second SVD multiply by a factor of 5. Panel B show the corresponding kinetic traces for the two SVD.	71
Figure 4.4.	Normalized (negative) data comparison between the first SVD component of the Fe ^{III} sample and the ferrous (Fe ^{II}) minus ferric (Fe ^{III}) steady state spectra.	74
Figure 4.5.	Normalized data from the rHbI Fe ^{III} sample at long time scales. The first “group” at 422 nm corresponded to 4.33-7.66ps. The green and pink traces correspond to 9.33 and 14.0 ps,. There was a red shift with time on both signals (bleached and induced absorption).	74
Figure 4.6.	Panel A show the first two SVD components of the ferric rHbI sample. The red dotted trace is the second SVD component multiplied by a factor of 10. Panel B shows the kinetic traces of the two signals.	75
Figure 4.7	Comparison between the Oxy minus deoxy Fe ^{II} rHbI sample and the SVD2 component of the Fe ^{III} sample analysis. (SVD component was multiply by its singular value).	75
Figure 4.8.	Comparison between the SVD-I component of the ferric-H ₂ S sample and the steady state difference spectra between the ferric-H ₂ S and the ferric sample.	78

Figure 4.9	Transient spectra of the ferric-H ₂ S sample at long time scale.	78
Figure 4.10	SVD 1 and SVD2 of the Ferric-H ₂ S sample compared with the ferrous minus ferric and the Oxy minus ferrous steady state spectra.	79
Figure 4.11	Panel A show transient absorption signals for the rHbl-H ₂ S sample at different delay position. Panel B show the kinetic traces at various wavelengths for the rHbl H ₂ S sample.	79
Figure 4.12.	First SVD transient component for the 4 different samples (3 new 1 old).	82
Figure 4.13.	Steady state normalizes modeling difference spectra of a ration combination of the Fe ^{III} , H ₂ S and Fe ^{II} species against the H ₂ S spectra.	82
Figure 4.14	Normalize model steady state different spectra where the rHbl-H₂S contribution is constant and the other two changed.	84
Figure 4.15.	Normalize model steady state different spectra where the rHb-Fe^{II} contribution is constant and the other two changed.	84
Figure 4.16.	Comparison between the first SVD transient absorption spectra for three H ₂ S mutant complexes.	87

List of Abbreviations

Hb	Hemoglobin
Hbl	Hemoglobin I
Mb	Myoglobin
rHbl	Recombinant hemoglobin I
<i>L. pectinata</i>	<i>Lucina pectinata</i> (Gmelin 1791)
O ₂	Oxygen
H ₂ S	Hydrogen sulfide
Phe	Phenylalanine
Gln	Glutamine
His	Histidine
RR	Resonance Raman
NO	Nitric oxide
CO	Carbone monoxide
CCD	Charge couple device
ICCD	Intensified charge couple device
FPLC	Fast performance liquid chromatography
TB	Terrific broth
dO ₂	Dissolved oxygen
nm	Nanometer
KHz	Kilo hertz
OD	Optical density
fs	Femtosecond
ss	Steady state
WL	White light

®2011 Cacimar Antonio Ramos Álvarez

1. Introduction

Since the discovery of myoglobin and the elucidation of its structure, heme proteins have been studied extensively, due to their essential and widely spread role in many biological systems. Despite their apparently simple ligand reaction, research has revealed many levels of complexity associated with this process. Besides all the work done there are still many aspects of their ligand binding mechanism, that are not fully understood. Recent efforts have been focused on the study of invertebrate hemoglobins due to their similarity to heme proteins from higher organisms, including humans and for their availability.

Several invertebrate hemoglobins are found in the clam *Lucina pectinata* (Gmelin 1791). This tropical clam is collected in sulfide-rich mud in the coastal mangroves of the southwest coast of Puerto Rico. *Lucina pectinata* contains three different hemoglobins within the gill tissue. Those proteins are called hemoglobin I, II and III (HbI, HbII and HbIII, respectively) each one characterized by distinct physical-chemical properties. The first, HbI, is a monomeric protein of 142 amino acid residues, and is responsible for oxygen and/or hydrogen sulfide transportation. It is comparable in size to several vertebrate oxygen carrier myoglobins and is considered by some as a naturally occurring myoglobin mutant (1). This heme protein exhibits fast combination rate with oxygen (1) and is the only known heme protein that binds H₂S in the active site center. The transport mechanism and intermediate steps for the ligation and dissociation of the different ligands are almost unknown. Many of these mechanisms involves short-lived intermediates that can only be observed using ultrafast techniques. By using ultrafast

absorption techniques we studied the first steps in the binding and braking of the ligated heme species.

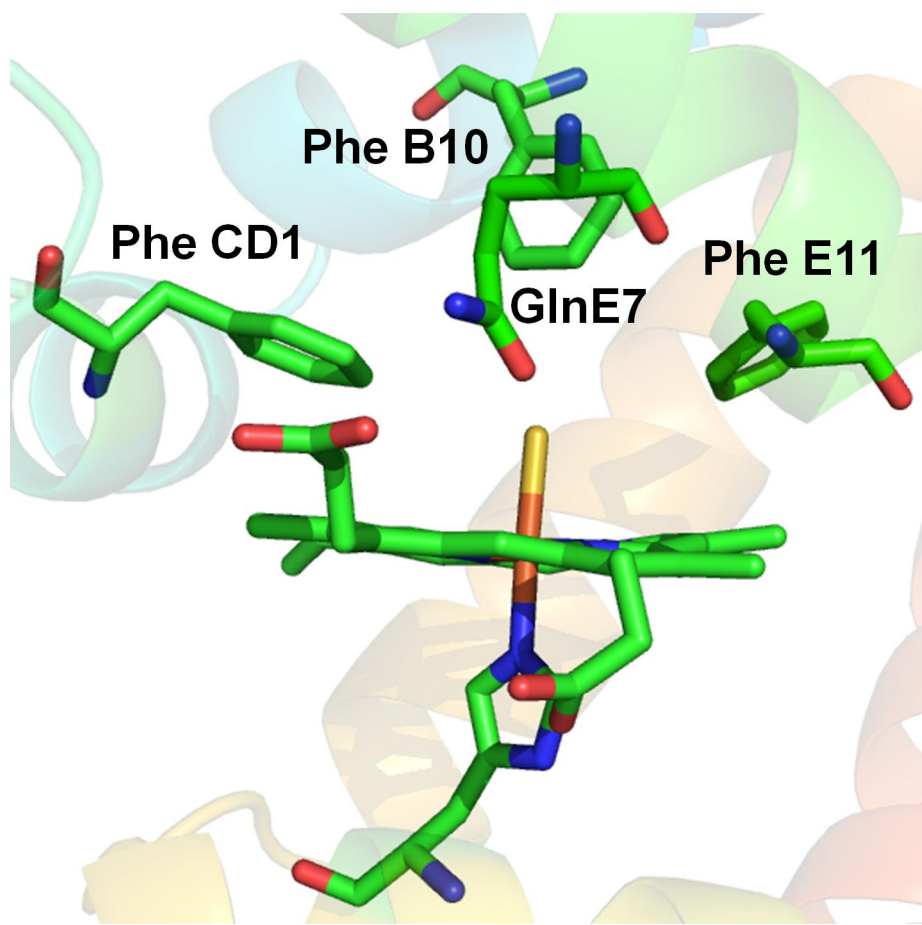


Figure 1.1. Hbl reactive center, showing the residues around the distal and proximal positions.

The HbI heme-pocket structural organization was elucidated using x-ray crystallography (2, 3). The molecule shows a peculiar arrangement of phenylalanine residues Phe (29) B10, Phe (43) CD1, and Phe (68) E11) and a glutamine (Gln (64) E7) instead of the highly conserved vertebrate histidine (His (64) E7) (Figure 1.1). The ligand binding and electron transfer properties of HbI may be influenced by the low distal pocket polarity and the aromatic nature resulting from this array of phenylalanine residues. The measured distances based on the crystallographic data revealed distances between the pocket residues and the metal center varying from 3.28 to 3.80 Å, with the ligand fully inaccessible to the solvent. It is presumed that the size of the distal residues is not the main factor controlling ligand-bound structures and the ligand binding kinetics, but rather electrostatic forces which play the major role. Since it has long been known that the conserved heme pocket amino acids in vertebrate heme-proteins modulate the ligand-binding properties and hence their function, it was suggested that the ligand-binding properties of HbI was related to its unusual heme pocket amino acids (4). Indeed, several resonance Raman (RR), proton nuclear magnetic resonance (^1H NMR) and infrared spectroscopic studies of different HbI derivatives have suggested that synergetic effects of the aromatic residues and the Gln (64) E7 modulate the ligand-binding properties in this system (5-8).

Recent developments in molecular biology have allowed the study of the effect of the heme pocket residues, by mutating them and observing how various properties of the protein change as it binds and releases diatomic molecules. Site directed mutagenesis takes advantage of the development of bench-top bioreactors and the use of various strains of bacteria, *E. Coli* BLi5 in our case, to generate high quantities of

recombinant and mutant heme-proteins. This technique and the expression of recombinant hemoglobin I (rHbl) and Hbl mutants provide the opportunity *a priori* to generate specific mutations in the active site of the heme protein (6). The meticulous process, offers unique samples impossible to obtain otherwise. The process takes approximately four days of preparation prior to the fermentation protocol and one more week for extraction and purification of the protein. The final volume after the purification protocol is about 10-40 mL with a concentration of ~50-100 μ M. If sample- demanding experiments needed to be performed the total protocol would need to be repeated several times for each desired protein. Based on Hbl characteristics and almost unique ligand reaction with H_2S , NO, and O_2 , the study of Hbl, rHbl and Hbl mutants presents a fascinating model for invertebrate hemoglobin investigation.

The applications of ultrafast time resolved spectroscopy to biological systems has received much attention in recent years (9-11) because many biochemical reactions, that include bond breakage, energy dissipation, molecular motion, and structural and chemical changes are occurring in a few femtosecond (fs) to picoseconds (ps) time scale. In recent years, the definition of chemical reaction has evolved from the simple reactant-to-products scenario to a more realistic scheme in which a chemical reaction occurs in a successive series of steps, involving various short-lived intermediated species. The study of chemical reactions has moved from a macroscopic treatment of empirical kinetics to a microscopic molecular viewpoint of chemical dynamics. Ultrafast time resolved absorption spectroscopy experiments are based on the pump-and-probe scheme. Time resolution is obtained by delaying one pulse of the desired wavelength with respect to the probe beam that is most often within the visible

spectrum region. Thus, to determine the dynamic events of a particular reaction the change in sample absorption is obtained as a function of the distance difference traveled between the two beams, which later is translated to time using the light velocity constant ($c = 3.0 \times 10^8$ m/s). The binding of various diatomic molecules like CO, O₂, and NO with heme proteins has been extensively studied by ultrafast time resolved spectroscopy since they can bind to the iron active center and give information about electronic structure of the protein active site.

In recent years another small molecule has also emerged as an interesting ligand for heme protein. The gas molecule H₂S previously known for its characteristic odor and toxicity has been noted as an important physiological mediator with a wide variety of roles in the human body. It has been found that H₂S is produced in mammalian tissues and that similar to nitric oxide (NO) and carbon monoxide (CO) it may function as a neuromodulator, neuroprotector and/or smooth muscle relaxant/constrictor (22). The hemoglobin I from *L. pectinata* offers an excellent scenario for the study of those reactions with H₂S as its natural ligand.

For instance, the elucidation of the factors controlling small molecules discrimination in mammalian hemoglobin and myoglobin is an area of increasing active research (4, 6-7, 9-11, 15-17). The growing data in the ultrafast time domain has revealed complicated photophysics of the heme that are sensitive to both, structure and to the ligand intrinsic identity. The time-resolved absorption spectrometer used by Petrich, *et al.*, (10-11) comprised of a colliding-pulse, mode-locked ring laser whose pulse were amplified to 1 mJ at 10 Hz with a Nd:YAG laser. Their femtosecond time scale experiments on human hemoglobin showed the formation of two short-lived

species after the absorption of a visible photon by the heme. These species were called Hb_i^* and Hb_{ii}^* and have been assigned to electronic excited states of the deligated heme. It was observed that both species were formed in less than 50 fs from the photoexcited Hb-X specie (X denotes the ligand). The lifetime of Hb_{ii}^* is determined to be 2.5 ps as measured at the maximum absorption peak at 450 nm. The Hb_i^* state corresponds to an intermediate in the pathway to the ground state unligated heme protein. During this process a deoxy-like specie is formed with a time constant of approximately 300 fs (10-11, 16). Ligand binding then occurs with these species and induces changes in the Fe spin state, in the porphyrin structure and in the protein conformation, all of which are relevant for the study of the biological function and binding mechanism of this heme protein.

However, the use of biological samples forces a series of constraints when developing the experimental setup for such experiments. These samples are frequently sensitive and can be photo-degraded easily. Normal pump-and-probe experiments involve the use of two laser beams that overlap on the sample. One of the beams called the pump excites the sample and a second pulse; the probe interrogates or tests the sample. Before studying samples the time coincidence of these two beams (pump and probe) is determined, and is designated as the “time zero”. This position is determined experimentally when both beams overlap in time and phase on the sample. This experiment besides being the basic for future measurements also helps to determine the cross-correlation of the pump-and-probe pulses on the sample. The easiest approach is the use of a photodiode coupled to a lock-in amplifier to measure the difference in absorbance on the sample caused by the pump pulse as the function of

the optical delay position. A more elaborated and sensitive approach is the use of a photo multiplier tube (PMT) detector instead of a photodiode (18). This setup, similar to a photodiode, will generate a 2D plot where the x-axis is the time axis (usually in fs) and the y-axis represents the relative intensity (usually in arbitrary units [au]). The signal to noise ratio of this last setup gives excellent resolution but has the disadvantage that only one wavelength can be measured at once. A normal experiment of one heme protein, probing in five nm steps jumps, will take a couple of hours (5-7 hr) to be completed. As it should be expected, the laser and environmental condition for the experiments could change extensively over this period, which will affect the quality and quantity of the data (19). A better approach would be to use a charge couple device (CCD) detector where a range of wavelengths can be acquired simultaneously, resulting in more complete data, less laser exposure to the sample, and reduction in experiment duration. This project is thus focused first on the development of an ultrafast laser system setup for absorption measurements using a CCD detector. Second, ultrafast dynamic of Hbl and Hbl mutants with different ligands using femtosecond spectroscopy will determine the initial step in the interaction of this heme protein with its ligand molecules.

1.1 Specifics goals

The specific goals were to develop and construct a state-of-the-art ultrafast laser system suitable for working with biological samples. Second, a dynamic description was performed to determine the behavior of recombinant Hbl from *Lucina pectinata* towards the interaction with SH₂, its native ligand, using ultrafast absorption laser spectroscopy with CCD detection. The ligand binding mechanism and photo-dissociative intermediates species formed were elucidated, by the photo-excitation of these heme proteins. Lastly, the ultrafast kinetics and dynamics view were examined and compared with the thermodynamic steady state model for SH₂ proposed by our research group (22).

1.1.1. Goal 1. Optimize the mutant expression protocol to generate higher quantities of the desired recombinant protein. The “scale up” process for protein generation using molecular biology techniques was optimized to improve the yield of protein expression. The original process was developed for small batch volumes and needs to be optimized for large-scale bioreactors. The developed process using fermentation flasks, although useful, does not maximize the reactive resources and protein expression. When exporting a method from a small volume beaker to a bioreactor, there are many parameters that needed to be controlled simultaneously (e.g. pH, dissolved O₂, agitation, temperature, glucose feeding, etc.) to generate a suitable environment for the over-expression of the desired recombinant proteins.

1.1.2. Goal 2. To incorporate a 3D detection system and fast data acquisition. In our efforts to evolve from a single wavelength setup to a multi

wavelength setup, an intensifier charge-coupled-device (ICCD) detector was incorporated into the detection system. This detector is capable of acquiring a wide range of wavelengths (λ) at a single delay position instead of just one measurement per position. This creates a 3D overview of the heme system under study. The 3D plot shows an intensity surface matrix which is a function of three parameters; wavelength (λ), time (fs or ps) and signal intensity (arbitrary units [au]). This “surface” give us the opportunity to extract the kinetic data of the sample at any particular wavelength. It allows the global analysis to fit the data where the contribution from various wavelengths are considered at once. This provides a more accurate overview of how the evolution from ligated to unligated takes place, for these heme proteins, under the influence of the pump beam.

1.1.3. Goal 3. To create a software tool to merge the detection measurements with the time resolution of the experiments. Since the time resolution of the experiments is generated by an optical delay line, the detection system has to be coupled with this delay to resolve the experiments in time. This data must be hard coded so that a computer is able to control the acquisition of the data, the movement of the delay line, and the time conversion of the movement. This software must move and read the position of the optical delay line. Also, it must acquire data from the detector, save it rapidly, and be able to plot the data traces so that the user can monitor the progress of the experiment. This must be synchronized with the laser that registers the timing. Our laser system works at a 1 KHz repetition rate; meaning we should acquire one spectrum per millisecond or 1,000 scans per second.

1.1.4. Goal 4. To incorporate a double-beam setup for data acquisition.

Ultrafast spectroscopy depends extensively on the stability of the laser, and on many other factors unmanageable by the user; thus it is important to simultaneously record the reference and the signal from the sample. Using this approach, any fluctuation within the laser pulses will be present in both signals and when subtracted, a better signal-to-noise ratio is produced. This is important when working with these samples because the experimental signals can be buried within the experimental noise. This adds to the complexity of the detection software to deal simultaneously with two separate sets of data in real-time which introduce more constraint to the software developed and the system setup.

1.1.5. Goal 5. To develop and construct a suitable sample handling

mechanism. To use a double-beam approach, a new sample mechanism must be developed and constructed so that the sample moves perpendicular to the laser beam to avoid heating and photo damage of the samples. The approach was to move the sample relative to the laser beam at a velocity such that each pulse hit a untouched spot in the sample cell. The construction was simple, solid and precise so that no new random errors were introduced into the data acquisition.

1.1.6. Goal 6. Incorporate global fitting techniques for data handling and reduction.

Compared to the 2D experiment the amount of data that is generated using a CCD will increase exponentially. Under normal 2D acquisition three repetitions are acquired, each one consisting of ~200 delay positions, which roughly totals 600 points, at specific wavelength. This is averaged after the acquisition generating only one trace at his specific wavelength. Using the 3D approach there are 500 repetitions at each

delay position, with each acquisition being composed of 1,024 pixels (pixels can be changed to wavelength after monochromatic calibration), representing ~102 millions data points. Thus, a data reduction scheme was implemented. The incorporation of a singular value deconvolution was also used for data analysis.

1.1.7. Goal 7 To determine the dynamics description of the recombinant HbI from *Lucina pectinata* toward the interaction with H₂S. *Lucina pectinata* present an excellent scenario for the study of the initial step of the reaction of heme proteins with diatomic or simple molecules. Among those simple molecules H₂S has recently evolved as an interesting molecule; H₂S can bind to hemeproteins, inducing different responses that in turn modulate its cytotoxic and cytoprotective activities (22). In the ultrafast time regime the initial steps involved in the interaction of H₂S with the rHbI active site was determine. This data was also used also to constructed and developed the experimental setup.

2. Materials and methods

2.1. Wild type (wt)- Hbl and Hbl mutants preparation

The clams, *Lucina pectinata*, (Figure 2.1) were collected from the mangrove swamps in the southwest coast of Puerto Rico. The hemoglobin extraction, isolation and purification were achieved following the methods described in the literature with a few modifications (9). Briefly, the separation of hemoglobin I (Hbl) and hemoglobin II and III (HbII/HbIII) was conducted in a Hi Load 26/60 Superdex 200 gel filtration column using the AKTA FPLC system (Figure 2.2). Hbl was purified in a Fast Performance Liquid Chromatography apparatus (FPLC) with a DEAE Sephadex Fast Flow cation exchange column equilibrated with 25 mM ammonium bicarbonate buffer, pH 8.3. The purity of the proteins was confirmed by the presence of a single band in a sodium dodecyl sulfate polyacrylamide gel electrophoresis (SDS-PAGE).

For mutant samples an already-cloned cell culture frozen stock was obtain from the laboratory of Dr. Carmen Cadilla from the Medical Science Center of the University of Puerto Rico at Río Piedras. Site directed mutant Hbl was obtained by introducing the single amino acid substitution into the Hbl coding region that was obtained by RT-PCR amplification from the total *L. pectinata* gill RNA and cloned into the pET28(a+) vector. The Hbl mutants and the wild type recombinant proteins were expressed in *E. coli* *Bli5* cells transformed with the constructs described above. Two days prior to the large-scale fermentation, an overnight culture was grown in 1/10 volume of 50.0 ml using the Terrific Broth (TB) EZ mix media which contains kanamycin and chloramphenicol antibiotics for the selective grown of our cells (Figure 3). After 12 hr an aliquot of 1 ml was extracted from this beaker and re-grown



Figure 2.1. *Lucina pectinata* shells after the tridia was removed for protein extraction. The clams were collected on the mangrove in the southwest coast of the Puerto Rico island.



Figure 2.2. Fast performance liquid chromatography (FPLC) equipment used for the separation and purification of the different hemoglobins.

overnight in 50 ml of fresh TB media at 37.0°C in a water shaker bath (Figure 2.3).

After 12 hr, the total volume (50 ml) of the bacterial growth was inoculated into 500 ml of fresh TB media in a Fernbach culture vessel at the same temperature (37 °C). For the expression and scale-up procedure, a 5 L fermentor was used with a 1/10 ratio with 4.5L of fresh media. The fermentor media was prepared as described previously (9) with some minor modifications. Briefly, 54.0 g of tryptone, 108.0 g of yeast extract and 36.0 ml of glycerol were added to the bioreactor and filled to 4.5 L with distilled water. The sealed bioreactor was then sterilized to have aseptic conditions. After sterilization, the vessel was connected to the control unit and each tube was connected to its respective inlets and outlets. Next, all the sensors were calibrated and equilibrated to have the initial optimal conditions. Once the vessel was equilibrated and the temperature of the media was stable at 37.0° C, the vessel was inoculated with 500 ml of the sample from the Fernbach culture vessel. The duration of the fermentation process was approximately 12 hr. The media was then collected and centrifuged to separate the cells from the media broth. Collected pellets where stored in a -80.0° C freezer for further lysis and purification.

2.2 Optimization of the fermentation protocol: The fermentation protocol was optimized to generate a higher protein yield, optimize the use of reactant and laboratory resources, and reduce the total time to generate samples. The volume of glycerol added to the media (i.e. from 18.0 ml to 36.0 ml) was doubled from the previous protocol. The increase in glycerol fulfilled two goals, first it is used by the bacteria in the grown phase (i.e. *lag phase*) as a carbon source and secondly the use of glycerol inhibits the formation of byproducts (23) that are harmful to the bacteria and can alter

the sturdiness of the culture. The pH and dissolved oxygen (dO_2) sensors were calibrated using the equipment protocol. The optimized fermentation method involved the use of the “agitation/ dO_2 ” option of the fermentation equipment which controls how oxygen and air are supplied to the growth media. Initially the agitation of the media was changed from a pre-set lower value of 200 rpm to a upper value of 600 rpm to maintain the dO_2 readout value in the set point (35% dO_2). During this phase filtered air was purged into the media to help the aeration process and to maintain the dO_2 value within the set point value. When the upper agitation value (600 rpm) was reached and the amount of dO_2 in the media was below the set point, pure filtered oxygen in combination with air was injected into the media until the set point was reached. The fermentation system was capable of adjusting the ratio of air/ O_2 by opening or closing each respective valve to maintain the vessel in the proper ratio of gases. Using this method there was enough dO_2 in the growth media to prevent it from becoming a “limited reagent” for bacterial growth. Prior to media inoculation 500 ml of a buffer solution with 2.54g of magnesium sulfate heptahydrate ($MgSO_4 \cdot 7H_2O$) was added to the media along with ~4.5 ml de kanamycin (to reach final concentration of 50 mg/ml) and ~4.5 ml of chloroamphenicol (to reach a final concentration of 30 mg/ml). Magnesium was speculated to help stabilize the RNA (21) to overcome the stress induced in the culture when the IPTG (Isopropyl β -D-1-thiogalactopyranoside) was used to induce exogenous protein production by the bacteria. The optical density of the media was measured before inoculation and during the fermentation process. A growth curve was plotted to monitor the stability of the cell culture. The data provided a visual “map” of

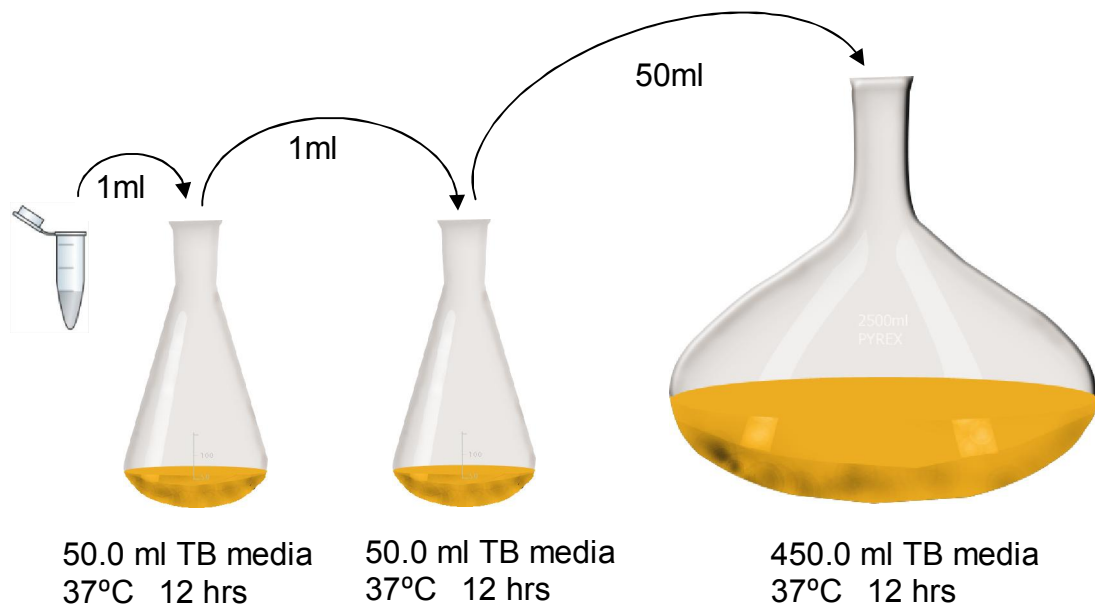


Figure 2.3. Pre-fermentation growth steps, for inoculation of the fermentor.



Figure 2.4. Fermentation system for bacterial growth and protein expression. It shows the control unit, the vessel, and the connections.

the culture growth stability and helped to decide when to start the glucose supplementation. When the optical density (OD) value of the bacteria culture reached a value of ~1.4-2.0 au protein expression was induced with IPTG. At this point hemin chloride ($C_{34}H_{32}ClFeN_4O_4$) was added to this media at a concentration of ~30 µg/ml to facilitate the incorporation of the prosthetic heme group by the bacteria on the recombinant protein. Temperature was maintained at 30.0°C because it helped in the incorporation of the heme group by the protein (9). The bioreactor system was self-controlled in terms of pH using an ammonium hydroxide solution (NH_4OH) as a base and potassium phosphate dibasic (K_2HPO_4) as an acid to maintain a value of pH ~7.5 during the process. At each optical density (OD) measurement, the pH of the aliquot was measured with an external pH meter to verify or correct any variations of the fermentation system unit measurement. The dO_2 was monitored in the system screen to correlate its behavior with the culture growth and stability. When the value of the dO_2 was below the set point (having the aeration and agitation at maximum), this indicated a deprivation of the carbon source on the vessel, and the culture medium was enriched with a 50% by volume glucose ($C_6H_{12}O_6$) solution at a 100% injection rate. The rate of glucose injection was further adjusted (values < 100%) as a function of the readout value of dO_2 on the system control unit. The supply rate of oxygen was adjusted automatically according to the dO_2 reading to maintain the vessel oxygenation level close to the dO_2 set point value of the media. The fermentation process was stopped when three consecutive OD measurements were similar, within the experimental error, the glucose had been consumed and the dO_2 level was close to the set value with the intake of oxygen at its lower value. The pellets were collected after centrifugation for 20

min at 3,500 rpm at 4.0° C and the supernatant was discarded. The wet precipitant pellet was stored at -80°C until further protein purification. Typical yield with the improved method were around 500-600 g of wet cell pellets, compared with ~50 g using the old method (27). The new method represents almost a 5-fold improvement when compared with the old one which translates to an easier, faster, and higher protein-yield production.

2.3. *Protein extraction and purification:* The storage pellets were lysed, in the presence of lysozyme and protease inhibitor, incubated for ~30 min at 0°C in an ice bath and centrifuged at 3,500rpm to separate the soluble protein from the insoluble cell fractions. The recombinant protein contained a histidine tag (His tag) system allowing the protein to be purified using a Co⁺² affinity columns (Talon, Invitrogen.). Further purification of the mutants was achieved using a FPLC with a Hi Load 26/60 Superdex 200 gel filtration column. The purification of the proteins was verified by SDS-PAGE analysis. The collected purified protein was concentrated and the buffer exchanged using a Millipore® filtration system under nitrogen (N₂) atmosphere.

2.4. *Complex Formation:* The complex derivatives for the samples was prepared by adding an excess of sodium dithionite (sodium hydroxysulfate) or sodium ascorbate under anaerobic conditions followed by exposure to the diatomic gas atmosphere (NO, and O₂). For the deoxy sample the same procedure was followed but the sample was maintained in a sealed N₂ atmosphere. A homemade tonometer system was constructed, consisting of a stainless steel manifold (4 [$\phi=3/8"$ id] and 2 [$\phi=1/2"$ id] inlet/outlets) connected to a vacuum pump, a pressure/vacuum gauge, a nitrogen gas line and any other gas line, if needed (Figure 2.5). Each $\phi=3/8"$ manifold connection has

a needle control valve connected that allows for the precise control of the gas and vacuum exposure of the sample. After preparation the identity of the complexes was verified by UV-Vis spectra which showed distinctive bands (Figure 2.6). Similar procedures were followed for the preparation of the H₂S complexe, with small modifications. In such case, a stoichiometric amount of sodium sulfide anhydrous (Na₂SO₃) was dissolved in a previously degassed buffer solution under anaerobic conditions. Then a volume of ~10 µl of this solution was added to the degassed Hb sample (~100µl). The complex formation and integrity was monitored with a UV-Vis spectrograph. Figure 2.6 shows the rHbI complexes with their characteristic absorption bands. The spectrum only shows the solet region of the UV-Vis spectrum.

2.5. *Instrumentation and data acquisition*

There were two instrument settings for these experiments. The first one was constructed and developed in the Chemistry Department of the University of Puerto Rico at Mayaguez; and the second system was utilized in the Laboratoire d' Optics e Bioscience (LOB) at the Ecole Politechnique in Paris, France.

2.5.1. UPRM UltrasFast laser spectroscopy setup. For the experiments at the UPRM laboratory, a Spectra Physics laser system was used. Initially a Ti-Sapphire oscillator was pumped with a diode array double frequency visible laser with a wavelength of 532 nm (Millenia) and a repetition rate of ~1 MHz. The output from this laser was further enhanced with a regenerative amplifier (SpitFire). This output was combined with the output of an YLF rod solid matrix laser (Merlin) with a wavelength of 527 nm and a repetition rate of 1 KHz. After “mixing” both beams on a Ti-Sapphire rod inside the regenerative amplifier and after the threshold power was reached, the output from the



Figure 2.5. Homemade tonometer system for sample degasification and complex-preparation. The system included a vacuum pump a manifold, several control valves, and a pressure/vacuum gauge.

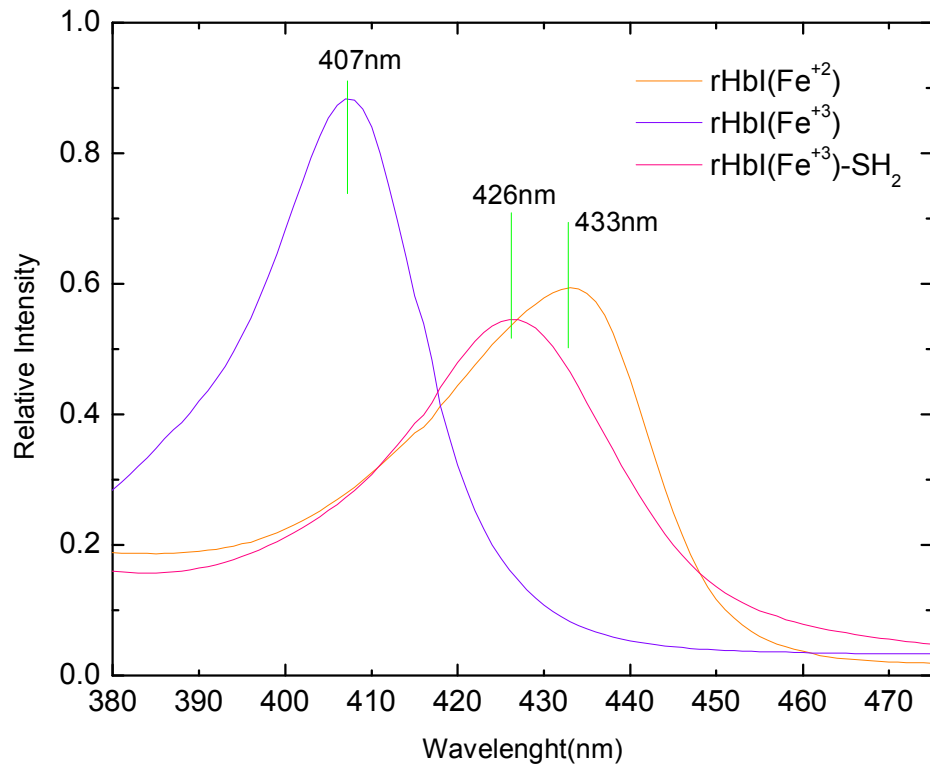


Figure 2.6. UV-Vis soret region spectra for rHbI complexes,(Orange-Deoxy sample, Purple- Metaquo sample and Red- H_2S complex).

the regenerative amplifier had a repetition rate of 1 KHz, 850 μ J of power at 800 nm wavelength. This beam was further divided into two separated beams using an 80/20 beam splitter. For this setup one beam was used as the pump source and the other as the probe beam. The 800nm pump beam had its frequency doubled in an LBO crystal to generate 400 nm wavelength emissions.

The second beam of 800 nm was focused on a sapphire window to generate a white light (WL) continuum beam used as the probe. This probe beam was further divided into two separate equal beams using a “polka dot” beam splitter, one was used to generate the sample signal and the other was used as the reference background for laser fluctuation correction. One of the WL beams probes the sample and the other probes either the air or a sample-less spot within the cell. The pump and the probe beam crossed the sample at a small angle between them (~10 degrees). Only the probe beam continued its trajectory to be focused at the entrance slit of the TRIAX monochromator (Yvon Hobine) equipped with an intensifier charge coupled device (ICCD) from Andor Technologies. Special care was taken to ensure that the area illuminated on the sample by the pump beam was larger than the area of the probe beam so that all the probed area was energized before it was detected. As mentioned previously, the detection system was composed of an intensifier charge coupled device (ICCD) (Andor Technologies) with a 1024 x 256-pixel chip coupled with a photon intensifier ($\phi=18\text{mm}$). To control and synchronize the data acquisition, a trigger signal from the laser was used to feed the detector, so that the data was acquired only when there is a pulse of light crossing the sample. The detector was used on any of the

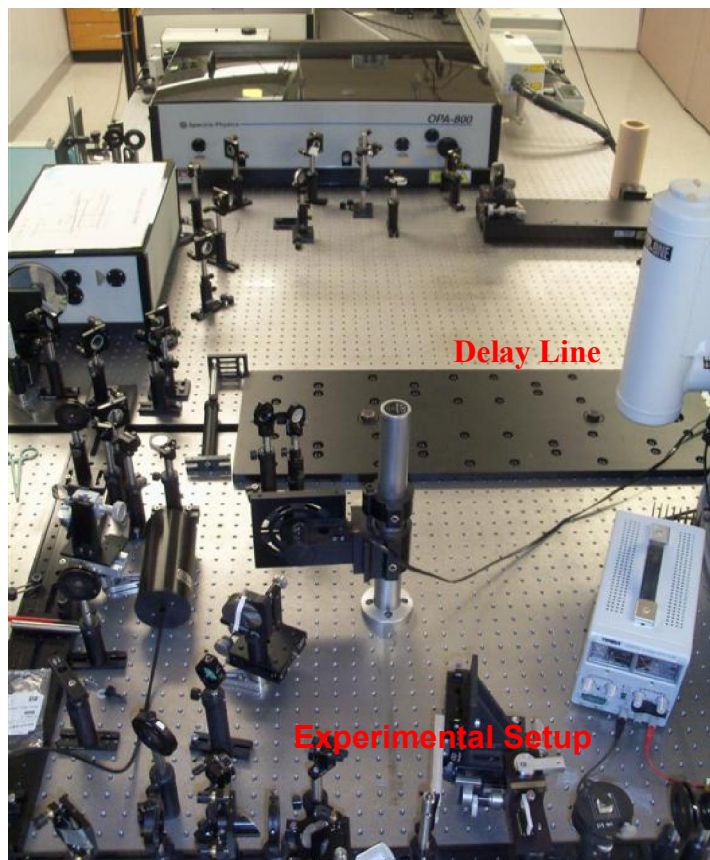


Figure 2.7. Femtosecond laser system, laser table and experimental setup area.

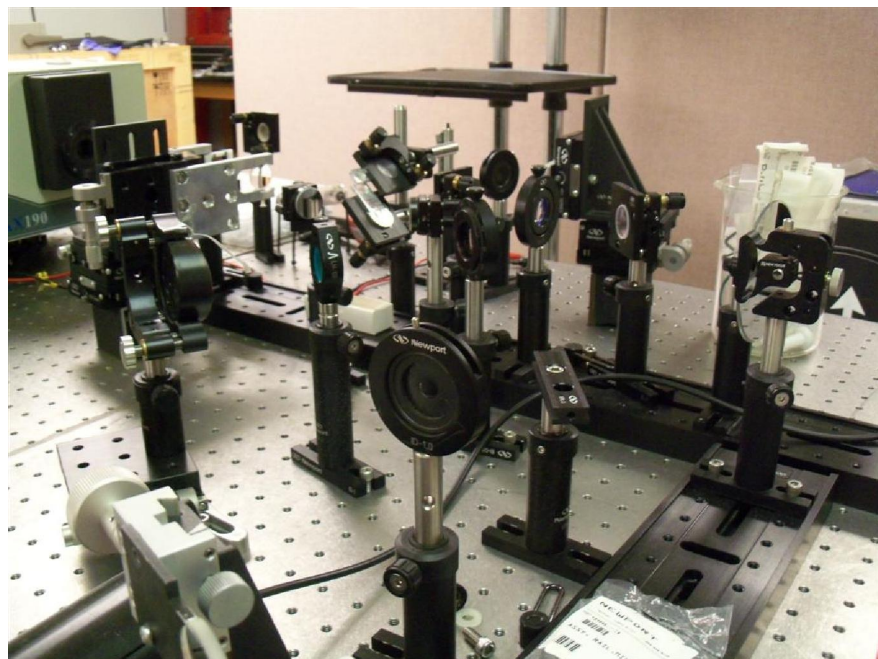


Figure 2.8 Experimental optical setup, sample, and detection area.

modes (full vertical binning, random track, multi-track and image) as long as a trigger signal was supplied, so the acquired data was as fast and accurate as possible.

2.5.2. Sampler cell holder and mechanism: For this experimental setup a sampler holding mechanism was constructed from scratch. To simultaneously acquire the sample signal and the reference signal a perpendicular approach with respect to the laser beam was used. Figure 3.8 shows the sampler holder mechanism with, a translational stage coupled to a motor so the rotating action of the motor moves the cell back and forth perpendicular to the laser beam. The movement was similar to that of the wheels of a train. The cell holder accommodated an 1.0 mm path-length UV-Vis commercial cell. The use of commercial UV-Vis cells adds versatility to the system because they can be found in various path lengths and materials, thus adjusting to the specific need of the experiments and samples.

2.5.3. Ecole Politechnique Ultra Fast Spectroscopy Setup The ultrafast laser system used in Paris, France is described elsewhere (24). A homemade dye ring laser was operated at 30 Hz and provided excitation and probe pulses of ~50 fs. Both beams were focused on a spot of ~50 μm and overlapped within the sample cell, which was continually moved perpendicular to the beam to avoid sample damage. For each laser shot, a reference probe intensity was measured and stored simultaneously with the probe intensity passing through the sample to calculate the absorbance change of the sample. The transient absorption was recorded on a CCD camera coupled to a monochromator. The group velocity dispersion (GVD) of the probe beam was compensated by a set of prisms.

2.6. Data Acquisition. After the sample was placed inside the UV-Vis cell and sealed with a septum, it was mounted on the cell holder and the motor was maintained at ~2.0 V so that the entire assembly moved perpendicular to the laser beam. This was made so that each pulse “probed” a new sample volume. The probe beam was first aligned and focused on the sample inside the cell into a small spot. The second beam, the pump, was aligned over the probe beam making sure its diameter on the cell was at least two times the size of the probe beam. The pump beam, after crossing the sample, entered into a “beam dump” to avoid it reaching the detector to minimize the scattered light. Another probe beam is focused on the sampler cell on an area without sample so that this beam could be used as the background signal. After crossing the sample both “probe” beams were focused on the entrance slit of the monochromator using cylindrical lens so that there were two visible, separately illuminated areas on the detector. The detector discriminated between the two areas, thus simultaneously acquiring a signal and the background spectra. Time resolution of the experiment was obtained by means of an optical delay line controlled with the acquisition software.

2.7. Software for data acquisition: The detector was coupled to an optical delay line by “hard-coded” software written in Visual Basic® 6. The software’s basic function involved the manipulation of the delay line, moving while recording its position, and controlling or receiving the intensity data measurements directly from the detector. Based on the particular needs and on the available hardware, the software includes simple tools that help in the preliminary data analysis after each run. The basic “flow chart” of the software code was to move the delay line and acquire full scans of the signal and the background at this position. Those two traces were later averaged; the delay then

proceeded to move to another position to continue acquiring data until a final position was reached. Each data acquisition included a sample and a background signal to further convert those measurements to absorbance (-log (signal/background)). The absorbance was correlated to the delay position with respect to the initial position to generate the time axis of the experiments. For each delay position transferred into the computer at least 1,024 intensity measurements (when used in FVB) per spectra with each experiment repetition was recorded. A run of 150 delay positions and 30 repetitions per position would translate into ~4.5 million points per run (1,024 pixels x 30 repetition x 150 delay position = 4,608,000 points). The data was saved as a binary file for computational velocity and space optimization. Pre-manipulation software tools provided preliminary views which included single spectrum visualization at different delayed positions and spectrum “slicing” so that transients at different wavelengths could be plotted and displayed. The data at each position could be exported to a Microsoft Excel[®] spreadsheet for future data handling and analysis. The software had the option to export the raw data (signal and background separate) or the absorbance to separate files. The analysis was made using Origin[®] software and its nonlinear curve-fitting capabilities.

2.8. *Data handling and mathematical fitting:* The data obtained in France was handled and fitted with a series of homemade software developed by the French group and written in Fortran computer language (24). Initially the data was viewed and averaged using the software they developed (Read4.exe). This data then was then transferred to a Singular Value Deconvolution (SVD) software that reduced the data to obtain the most significant components. The output from the SVD analysis generated three matrixes,

the first one that shows the singular values of the data from the most significant to the least significant values. The second matrix indicated the relationship between the wavelength and the intensity and; the third showed the relationship between the time and intensity. The intensity vs time traces were further analyzed using nonlinear exponential decay analysis with a homemade software. Since the acquired data has three time interval windows, the software must take this into account while trying to adjust data to the exponential model. The analysis gives numerical values for each of the components, indicating the pre-exponential values to the data and the residual analysis of the fit.

3. Results

3.1. The fermentation protocol was optimized to increase the protein yield of the recombinant proteins, to maximize resources and to reduce the total time for protein generation. Using the previously stated procedure as the starting point, variations of the media supplementation, delivery of nutrients and gas supplementation was performed. The first parameter changed was the glycerol supplementation to the media. After various trials, the amount of glycerol added to the media was doubled from 15.0 ml to 36.0 ml. Glycerol fulfills two important tasks; first it was used by the bacteria as a carbon source during the “*lag phase*” of cell growth and secondly, its metabolic transformation of it inhibits the formation of some byproducts which are known to harm the bacteria itself (23). Another major change was made in the agitation and gas supplementation to the media, which controlled the mass transfer of O_{2(g)} through the media. The fermentation process was run under the “agitation/O₂” equipment option so that the bioreactor control unit managed the agitation and the sparging of O_{2(g)} to the vessel. The old protocol involved the use of pure oxygen to aerate the media which increased the operational cost of each fermentation and exposed the bacteria to toxic hyperoxia environment decreasing cell yield and causing culture stability (23). Using the agitation/O₂ option, there was a constant injection of filtered air (21% O_{2(g)}) to help maintain the dissolved oxygen set point. The air/O₂ combination reduced the oscillation in the control system response, resulting in a more smooth oscillation around the set point. The dO₂ value was set to 35% to ensure the media was well oxygenated but not over oxygenated. During the run as the quantity of

B	Name	Value	Setpoint	Control
I	Temp	30.0	30.0	Auto
O	Agit	0	250rmp	Off
F	Pump A	0.0	50%	Off
L	Pump B	0.0	50%	Off
O	Pump C	0.0	50%	Off
1	pH	7.0	7.5pH	Auto
1	dO ₂	30	35%	Off
0	O ₂	0.0	100.0%	Off

Figure 3.1. Bioflo 110 fermentor control unit screen indicating the various parameters that can be monitored and changed during each run.

Parameters	Old Method	Optimize method
Glycol supplementation	15.0 ml	36.0 ml
Gas use for aeration	O _{2(g)}	Air/O _{2(g)}
dO₂ set point	100%	35%
Oxygenation Control	Agitation	Agitation/O ₂
Glucose addition	From start	When deprived of the initial carbon source (glycerol).
Magnesium	None	2.54g
Hemin chloride	15.0ml @ 30%NH ₄ OH	30.0ml @ 30%NH ₄ OH

Table 3.1. Summary comparison table between the old method and the improved method.

cells increased the dO₂ consumption also increased and the readout value of dO₂ decreased from the set point. As the control unit sensed this change, it opened the O_{2(g)} valve and injected O_{2(g)} to the vessel to increase the amount of dO₂ inside the vessel. The system is capable of injecting O_{2(g)} from 0%, this means only air is injected to 100% where only O₂ enters the vessel.

Because Mg⁺² ion can intercalate between the RNA bases stabilizing them (21) it is suitable for neutralizing the negative charge density associated with the RNA phosphate backbone. This is based on two characteristics. It, is the most abundant intracellular multivalent cation and has the highest charge density of all biological available ions (21). Since our protein expression and production involved “tampering” with the normal “machinery” of cell replication, we needed to compensate for the induced stress inflicted to the cell by the exogenous genetic material. Thus, we added 2.54g of MgSO₄•7H₂O to supplement the vessel before the inoculation of the media. The experiments were performed with and without MgSO₄•7H₂O. When the bioreactor was run without Mg⁺² enrichment, the OD values remained low however when Mg⁺² was added to the media, the OD values increased rapidly and the yield was 5-fold higher. To evaluate the effect of Mg⁺², MgSO₄•7H₂O was also added to te cell culture halfway through the experiment as shown in Figure 3.1. Based on these experiment, we

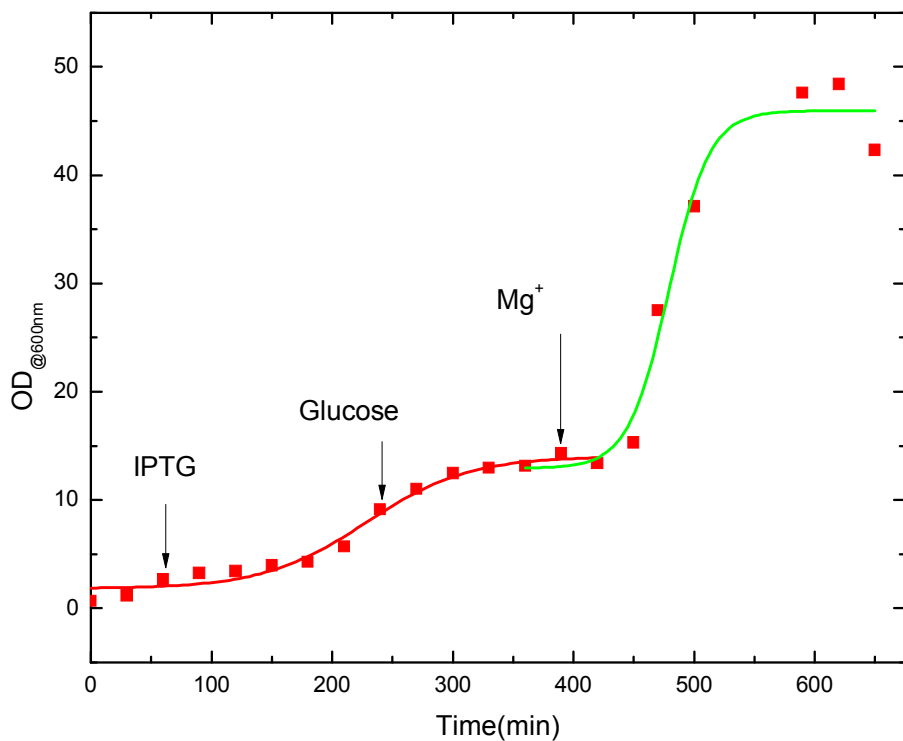


Figure 3.2. Growth curve for the experiment where Mg^{+2} was added halfway through the experiment. The first section indicates a lag phase at $\sim OD=10$; after the insertion of Mg^{+} the stationary phase $OD=50$.

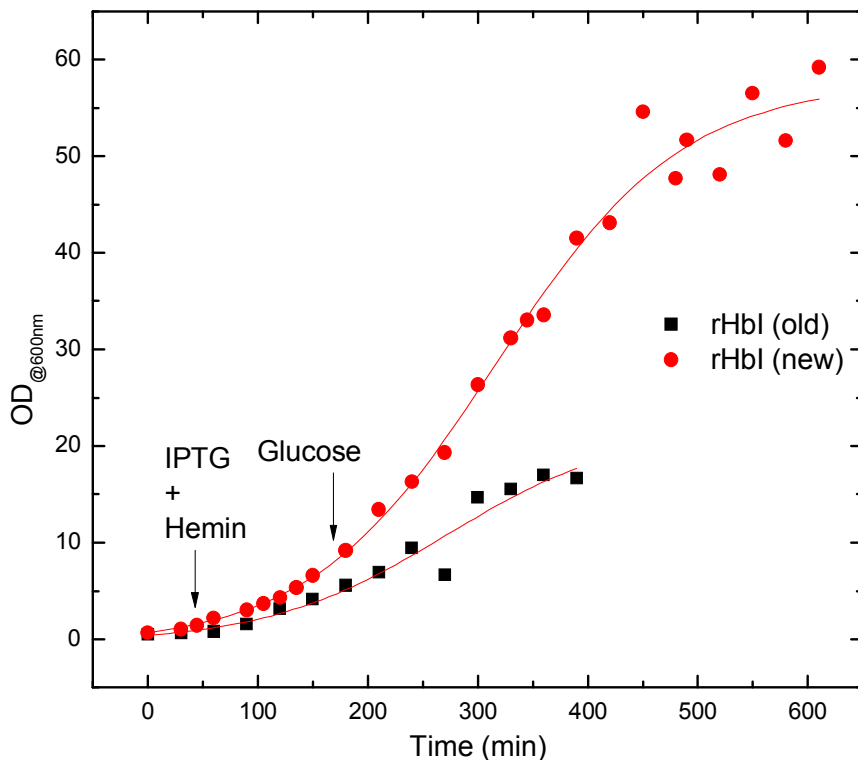


Figure 3.3. Bacterial growth curve for the recombinant Hbl species. The black trace indicates the old method and the red trace the new improved method.

concluded that from all the different adjustments and variations to the original methods the Mg⁺² enrichment was the principal contributor to the ultra-high yield obtained.

Figure 3.3 shows a comparison between the old and the new fermentation growth curve for some recombinant proteins (rHbl). It shows that the measured optical density increase of the new method which was roughly 4 to 5 times higher than the old protocol. The black trace shows the growth curve using the previous protocol with an OD of ~12-15 in the “stationary phase”. On the other hand using the new method (the red trace), an OD of ~55-60 was reached. During the fermentation run, each OD measurement was taken at least three times. The increase in OD translates into higher cell density in the media which increased the amount of protein we can extract from the cell pellet (~100-130 g/L of wet pellet). Table 3.2 summarizes the wet pellet yield for various expressed mutants using the old and the new method. Notice that some of them did not show any values; those mutants were grown with either one of the methods and not with both. In terms of mass, the improved method shows a five-fold increase. The new yields translated into less time in protein expression to generate the recombinant and mutant samples because one obtains sufficient quantities of cells for protein extraction and a better use of resources and reactants. However this does not imply that the cells were overproducing the protein. We increased the density of cells in the media so that the probability of having more protein-producer cells was increased and the yield therefore was increased. The new method opened the possibility for making high concentration-demanding experiments, such as nuclear magnetic

Mutant	Old Method	Optimized
rHbl	114 g	553 g
PheE11Val	116 g	583 g
PheB10Val		502 g
PheE11Tyr	46 g	
GlnE7His		474g
PheE11Gln	67g	

Table3.2. Wet pellet yield of the various worked fermentation process using the old and the new method.

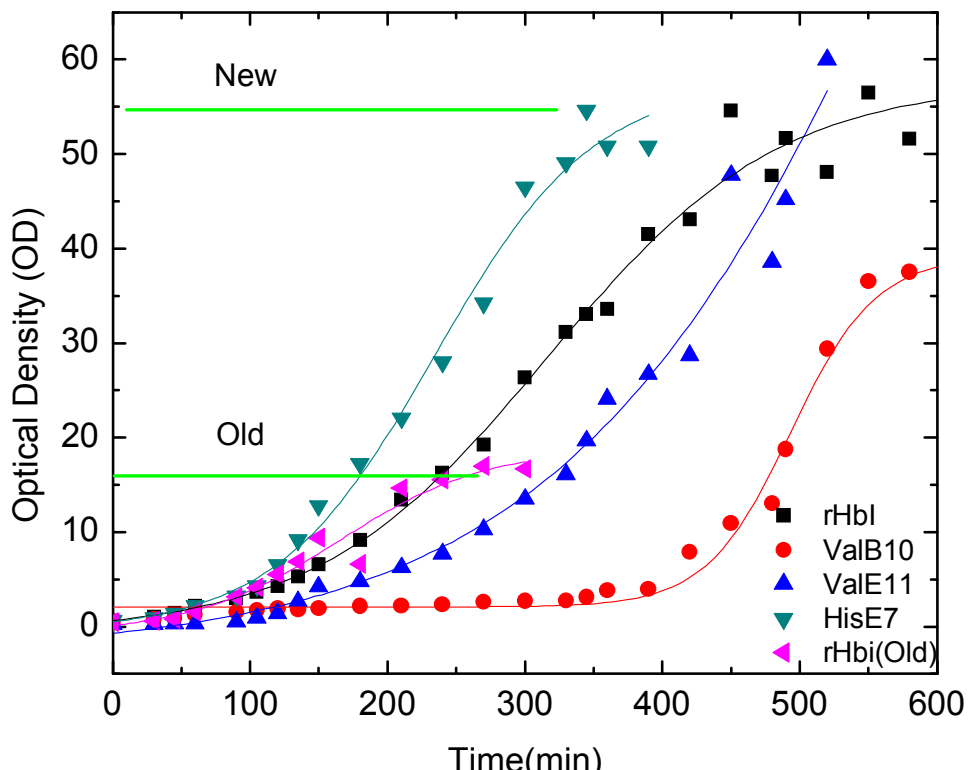


Figure 3.4. Growing curve for various mutants using the improved fermentation protocol. Black squares→recombinant HBI, red circles→ValB10 Mutant, Blue triangles→ValE11 and green triangles→HisE7.

resonance (NMR), infrared spectroscopy (IR) and continuous flow kinetic measurements, among others. The improved fermentation protocol was applied to various mutants, Figure 3.4, and another heme protein from the same organism with similar and promising results. Previously it was thought that expression and fermentation procedures were dependent on mutants; since some mutants were difficult to grow in the extreme bioreactor conditions. Figure 3.4 shows that all mutants reached at least an OD of 50 when run under the improved method. We concluded that the yield of each mutant was similar and the performance of the process itself, while in control, was similar. The minor variations of final yield between mutants were within the normal error range of the experiments.

3.2. Results Goal 2.

When working with ultrafast laser systems, there were no detectors available with electronics fast enough to acquire data within the femtosecond (fs) time frame. To be able to resolve the time axis for those experiments an optical delay line was used. Initially the first ultrafast systems used a photo multiplier tube (PMT) as the detector. Although the PMT offers the advantage of high sensitivity, only discrete wavelengths can be measured at once. The use of a detector such as a CCD or a diode array added the advantage of acquiring regions of wavelength at the same time (~100nm). We therefore added an ICCD detector (iStar DH720) to our TRIAX monochromator coupled to an optical delay line to obtain intensity (arbitrary units (AU) as a function of wavelength (nm) and time (fs, ps) (Figure 3.5). The detector, from Andor Technologies; had a 1024 x 256 pixel chip with a $\phi=18.\text{mm}$ intensifier couple to it. In addition, the detector has various working modes that included full vertical binning (FVB), multi tracks, and random tracks. FVB, sums each column vertically into one pixel, so one ended with a single 1,025 pixel row of information. Multi and random tracks divided the chip into various sections and used the information of those areas individually. The major difference between the last two is that in the random track, areas on the chip could be located allowing selection of the size with the only constraint that areas should not overlap. Under multi track, the user decides the number of areas to use and the system divided the detector chip equally between them. The selection of the different working modes needed to be added to the software so the user could select between modes. The program was coded in Visual Basic[®], the center core algorithm of the program instructions (Figure 3.6) was to move the delay line to the desired initial

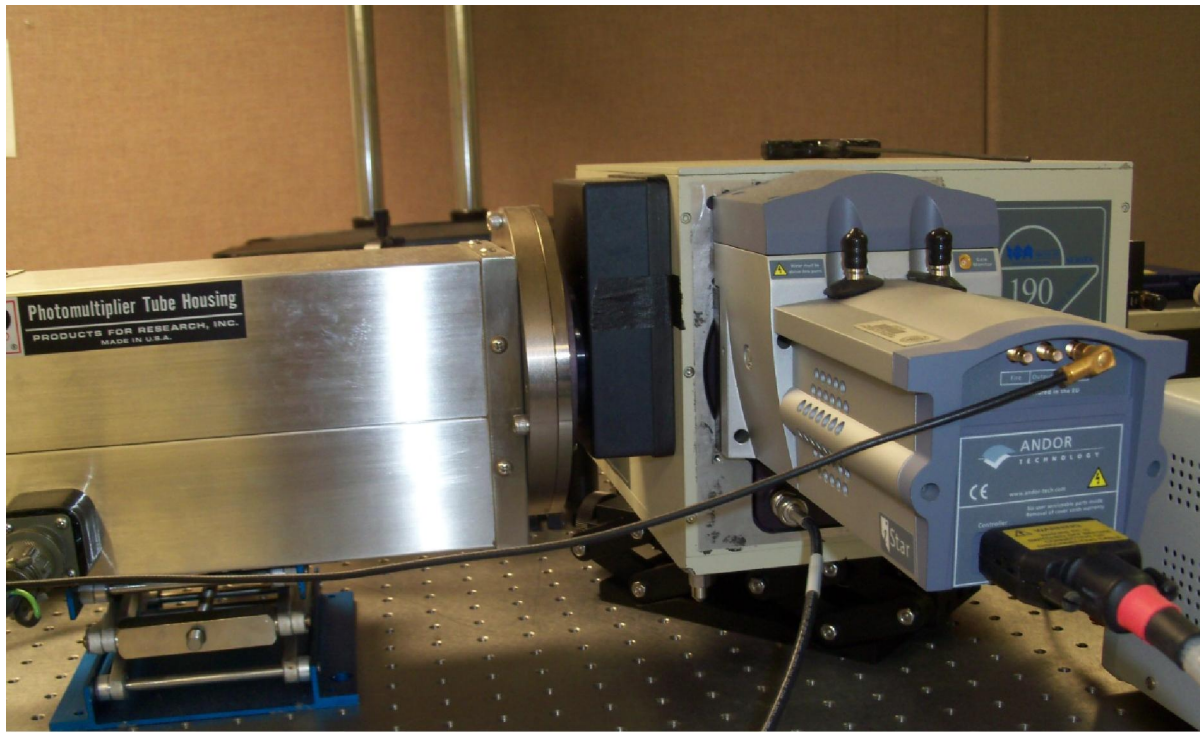


Figure 3.5. Intensifier couple device coupled to the monochromator for wavelength range acquisition.

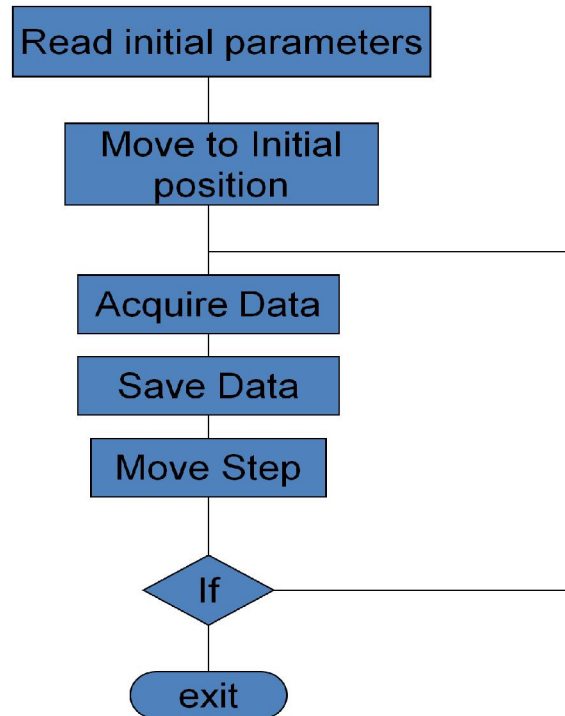


Figure 3.6. Software central core algorithm flow chart.

position acquire the data from the detector at that specific position and record both pieces of information, all this in a fast time frame and under the synchronization of the laser. This synchronization is crucial to the data acquisition due to the short pulses used and the repetition rate of the laser. To fulfill these tasks, more than 500 lines of code (Appendix 1) were written and a user interface was created (Figure 3.7). The user interface has 7 major areas. The first area (area I on figure 3.7) concerns the file management, name, and location of the file within the computer. The second area (area II on Figure 3.7) was designed for setting the initial parameter for the optical delay (initial position, final position, steps, and time zero position). These pieces of information have to be given prior to any run and will control the movements of the optical delay line. For simplicity, the input number for the position ranged from 1 to 150; each value was multiplied internally by 1,000 to change it to micrometers; for the optical delay controller. The position and delay information was used to calculate the time axis of the experiments. The subtraction of the actual position from the time zero position, multiplied by the “distance to time” conversion (using the velocity of light in vacuum) generated the time axis. The “time zero position” was experimentally determined prior to a sample measurement, in which the position of the pump and probe beams were synchronized in space and time. To determine this position, there were at least two methods; the sum of frequencies of the two beams on a BBO crystal (β -barium borate) and a dye (Rodamine G6) absorption saturation signal when both beams arrived simultaneously at the sample. The absorption change of the dye was measured as a function of the delay displacement. When a signal similar to a step function was observed, indicating the saturation of the dye by the pump beam producing that the

intensity of the probe at a specific wavelength increased. When the time zero is determined, the position does not change between measurements as long as nothing is moved on the laser table. This position value was used by the software to calculate the time axis from the movements of the delay line. The initial and final positions given to the software were dependent on the time zero position because the initial position is a value lower than the time zero and the end position will be a higher value. For every measurement, the absorption values were recorded before and after photo-excitation.

Area **III** in Figure 3.7 contains control parameters for the detector and various options that could be changed during each measurement. The first parameter on the list is the exposure time; with a default value of 0.001 ms since it is the fastest possible value. The next parameter is the number of accumulations per experiment, which varies (from 1 to 500). For the intensifier parameters, the “gain” value ranges from 0 to 100, the higher the number, the higher the sensitivity of the detector. The intensifier increases the number of photons similar to the PMT. The system could run using an internal trigger signal or an external signal such as the trigger signal coming from the laser so the acquisition was synchronized with the laser. Another important section controls the detector temperature to set the working temperature of the detector from room temperature to -20°C to reduce experimental noise. Area **IV** in Figure 3.7 is the plot area; the acquire data was plotted in absorbance mode. To accelerate the computational time, only even points (512 of 1024 pixels) are plotted. This reduces the time spent plotting the data, although each data point is saved in the file during the experiment. Area **V** on Figure 3.7 indicates how the detector was used; it has three major modes, FVB, Multi-track, and random-track. If random track is used, there is a

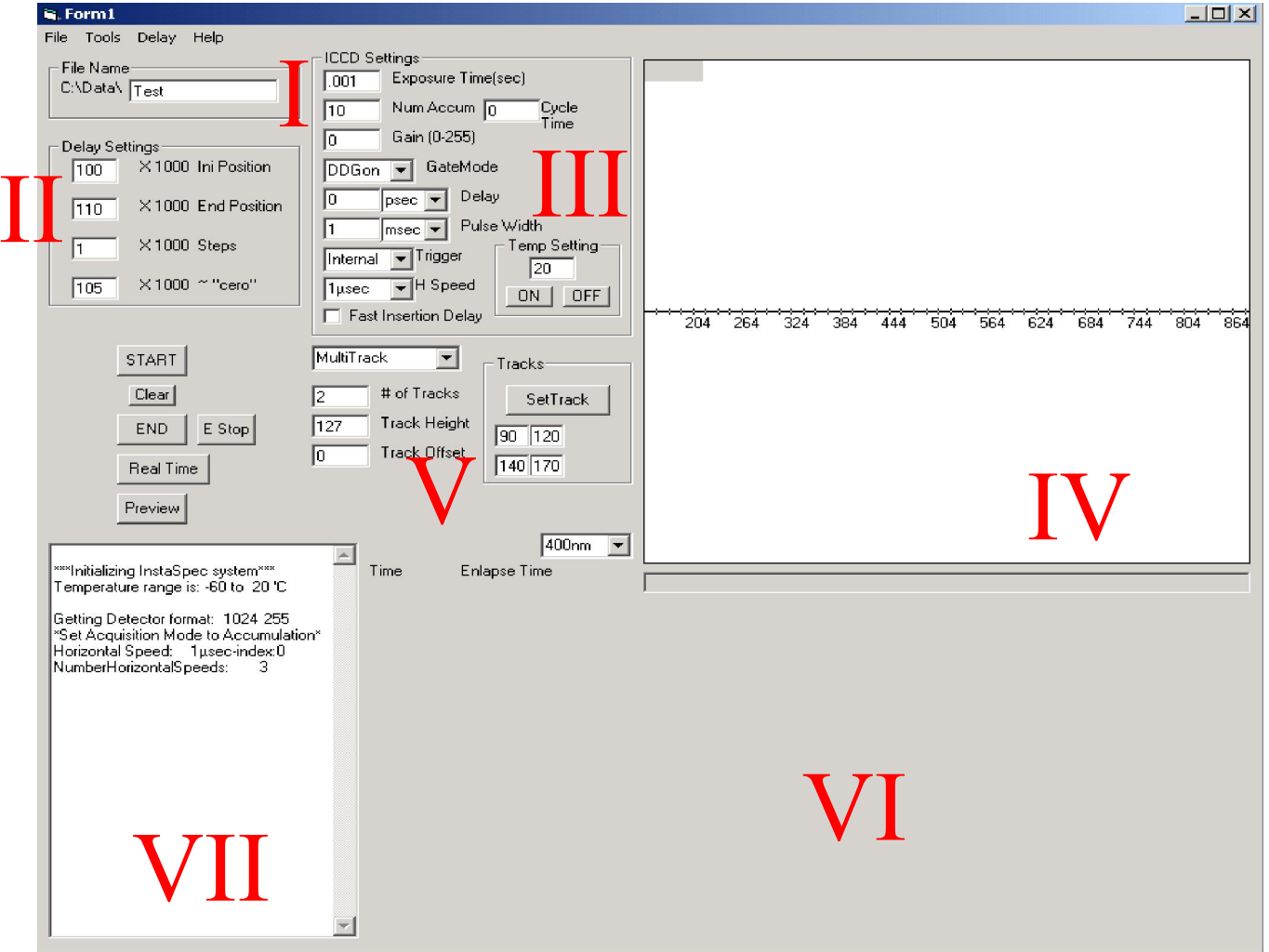


Figure 3.7. Software user interface windows with the different areas; **area I**-file name and directory, **area II**-Delay line parameters, **area III**-detector parameters, **area IV**-plot area, **area V**-Multi and random track settings, **area VI**-slice and transient specific transient absorption spectra plot, and **area VII**-notices window.

window where one could select the specific pixel used. Area **VI** in Figure 3.7 shows the intensity versus time trace at a selected wavelength, which provides information about the quality the data quality. Area **VII** on Figure 3.7 also shows the status of the detector and the delay line during the experiment, which allows to monitor the status of the instrument through the acquisition process. It also indicates error messages from the equipment.

Since the amount of data could be overwhelming and the analysis time-consuming, a software preliminary analyses tools were implemented to discriminate the quality of the acquired data, and laser beam stability. All the data was plotted on the graph area, which was programmed; so that the traces were “painted” and the scales were “drawn” according to the information from the optical delay line and the detector. One mayor constraint of the software and the coding was that the acquisition needed to be taken quickly, which resulted in fast data acquisition and handling. All the data was treated as binary numbers and the processing was performed after the data was acquired while the delay was moved to the next position. The use of binary numbers (zeros and ones) and binary files simplified the computational internal management and reduced the hard disk space used. A binary file can amount to 50-100 kilobytes while the same file using Excel[®] or a text file can take 10-20 times more space. Microsoft Excel[®] was the default option to export data, which limited data acquisition to 256 columns with 65,000 rows of data per sheet. It is important to mention that we could not acquire more than 128 delay positions when using the detector in “random track”. For each delay position two data columns are generated, one for the signal and one for the background, so 128 delayed positions are 256 data columns in .RAW mode or 128 data column in .ABS mode. After

the data is acquired it can be open in any spreadsheet software like Excel[®], Sigma Plot[®], or Origin[®], for further analyses and mathematical modeling.

3.3. Results Goal 3, 4, and 5.

For our experimental setup we incorporated a double beam array. We simultaneously acquired a sample and a reference signal to make a direct shot-by-shot correction of the data. Using this scheme, the noise was minimized and laser fluctuations were corrected, per pulse. Due to the hardware modification the light path on the laser table was modified. The probe beam was divided into two separate beams with a polka dot beam splitter (Figure 3.10-3.11), separating the beam ~50/50, one part passing through the beam splitter, the other half reflecting at 90° ascending angle. A second beam was reflected 90° again by an aluminum reflecting mirror located a few millimeters over the beam splitter in the direction perpendicular to the first beam (Figure 3.10). A base for holding the beam splitter and the mirror was designed and constructed. Both beams traveled perpendicular to each other until they reached the sample with one beam passing through the sample and the second through the cell glass without touching the sample.

To handle the samples in this two beam setup, we designed and constructed a sample-holding mechanism to move the sample cell perpendicular to the laser beam so that each pulse probes a new sample volume. For this new cell-holder mechanism, we used the train wheels principle in which a moving gear is connected off-axis to an arm and the rotational

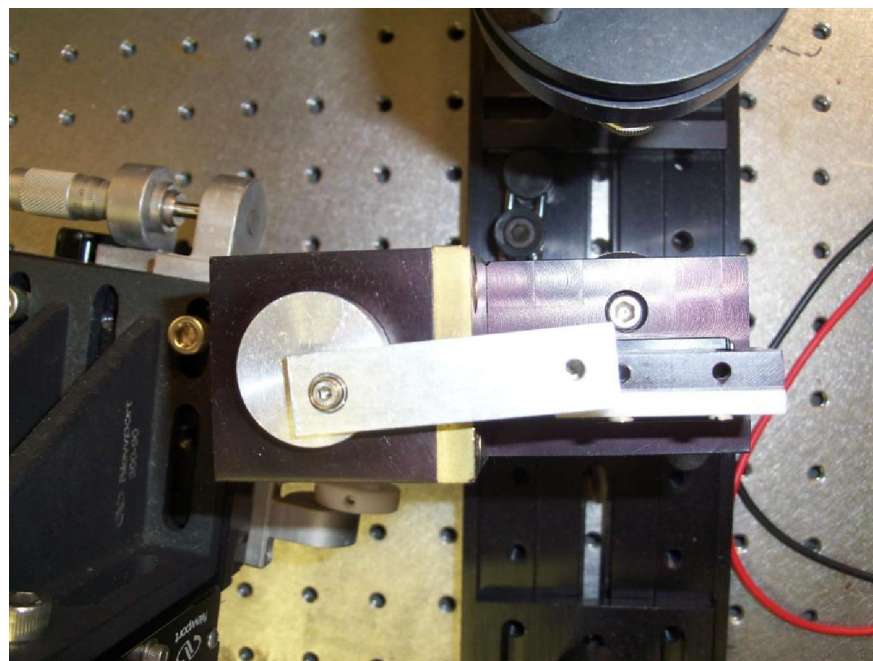


Figure 3.8. Designed cell holder, view of the moving mechanism.

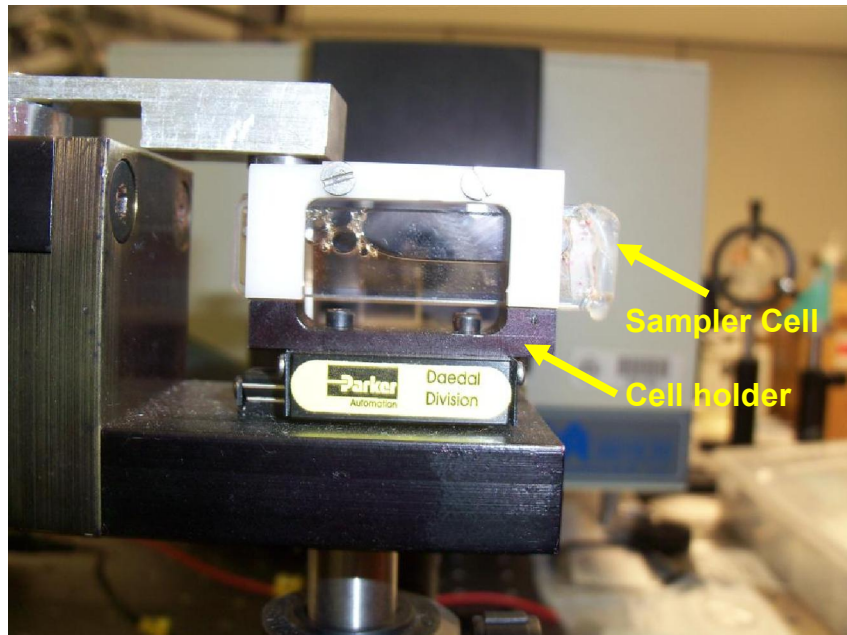


Figure 3.9. Front view of the cell holder mechanism and the sample cell. Notice how half of the cell looks filled with sample and the other part is empty.

movement moves the arm back and forward (Figure 3.8). The other side of the bar was connected to the cell-holder assembly, which is attached to a one-axis translational stage (Figure 3.9). This transferred the motor circular motion to a transversal translational movement perpendicular to the laser beam. Using this system; and changing the voltage applied to the motor that moves the gear, the cell can be moved and its velocity controlled. For this sampler handler mechanism, we used regular UV-Vis 1.0 mm pathlength cells which were placed horizontally on the holder. The cells could be sealed using a septum or other air-tight sealing methods when working with oxygen sensitive samples. Another advantage is the small sample volume required per run and the capability of leaving the sample under a moderate gas pressure when working with gas ligands. In this respect the amount of sample used per run during the experiments was around 100 µl so that when placed sidewise the lower section of the rectangular cell contained the sample and the upper part remained empty (Figure 3.9). The simplicity of the cell arrangement allows multiples cells sample to be used with different samples, avoiding cleaning the cells between measurements.

After crossing the sample area the two beams passed through a cylindrical lens (with focal length of 5.0cm) so that all the light information was “concentrated” into two distinct horizontal lines (Figure 3.10). Cylindrical lens were used to concentrate the light in one direction, horizontal or perpendicular. Both lines entered the monochromator through the entrance slit and were directed to the detector surface (Figure 3.10). The chip of the ICCD was divided into two sensitive and equally distributed horizontal areas (Figure 3.10). One area received the data from the interaction of the light with the sample and the other received the information of the interaction of the light either with

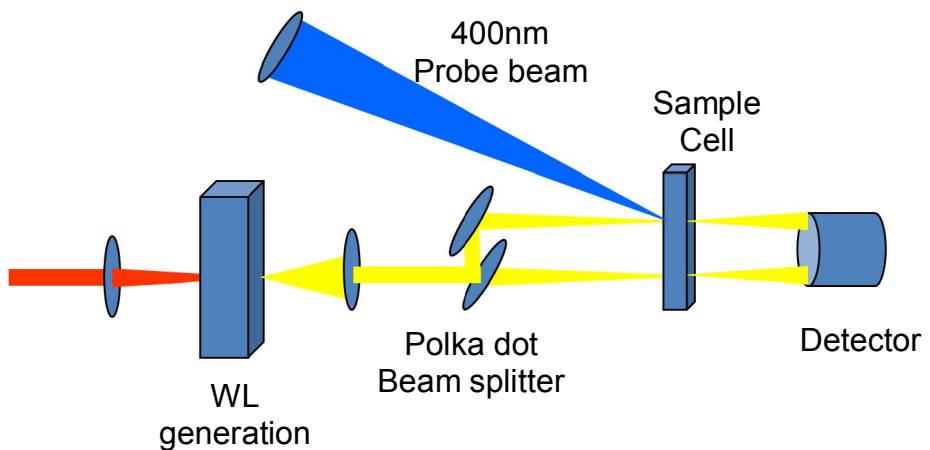


Figure 3.10. Double probe beam array sketch.

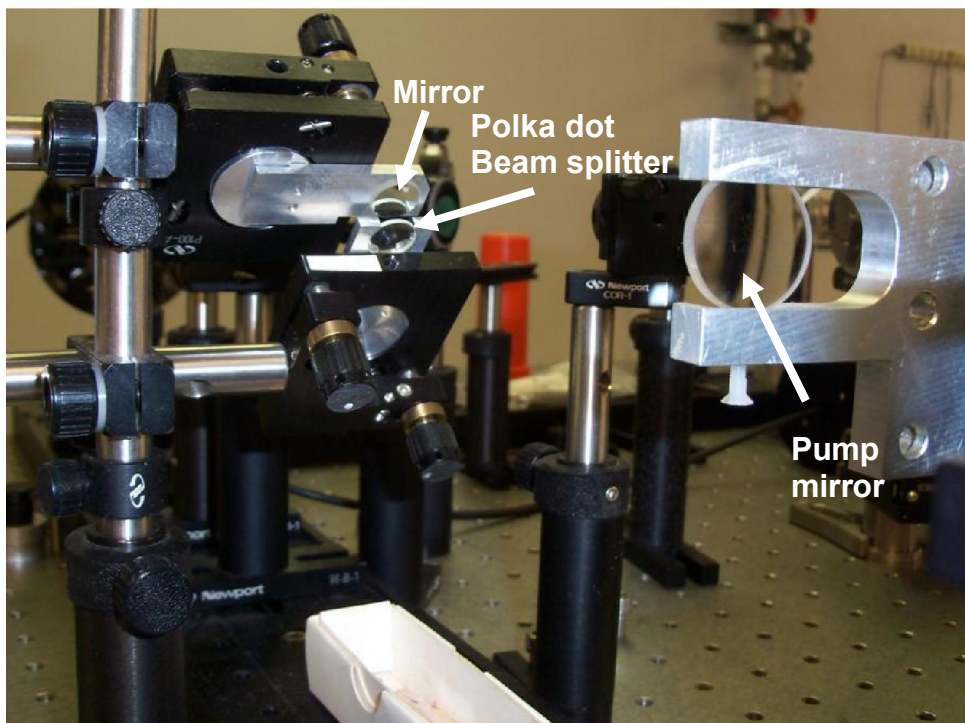


Figure 3.11. Picture of the laser table modification to accommodate a double-beam array. The beam-splitter and mirror mounting were home built.

the cell glass or the air. The collected data was mathematically manipulated to generate the sample absorbance in the specific wavelength range at the specific time by applying the logarithm of the rate of the signal against the background (-log(signal/background)).

Modifications were made to the original software version to add the random and multi-track options to programmatically separate both beams on the surface of the detector (Figure 3.12). Both sections were recorded separately and combined to calculate the data in the absorption mode. In Figure 3.13, the left side of the image (screen capture) shows the parameters used during acquisition and the spectral plot of the two areas. The two traces were not identical; since some of the light that passed through the sample was absorbed. Calculating the absorbance of the samples entailed obtaining the UV-Vis spectrum of the complex by calculating the negative logarithm of the ratio of the signal over the background. Using the detector image view (Figure 3.12) the user could see the specific areas of the CCD that were illuminated to collect data only from that region. For example, in Figure 3.13, two tracks are used, each one of ~30 pixels height. From a chip total height of 256 pixels only 60 pixels, would be used; the other 196 pixels would not contribute to the data. This could be useful when noise reduction is needed; because only information from the areas “exposed” to light would be recorded and black noise would be reduced. The two traces were plotted in real time so the laser stability could be determined by contrasting the traces profile on the screen. The computational cost was minimized by using binary numbers, showing only half the point in the graphical window and doing the mathematical calculation after the acquisition of the scans and not during the process. A real-time beam check was added to the software, allowing the user to verify the intensity of the two probe beams prior to

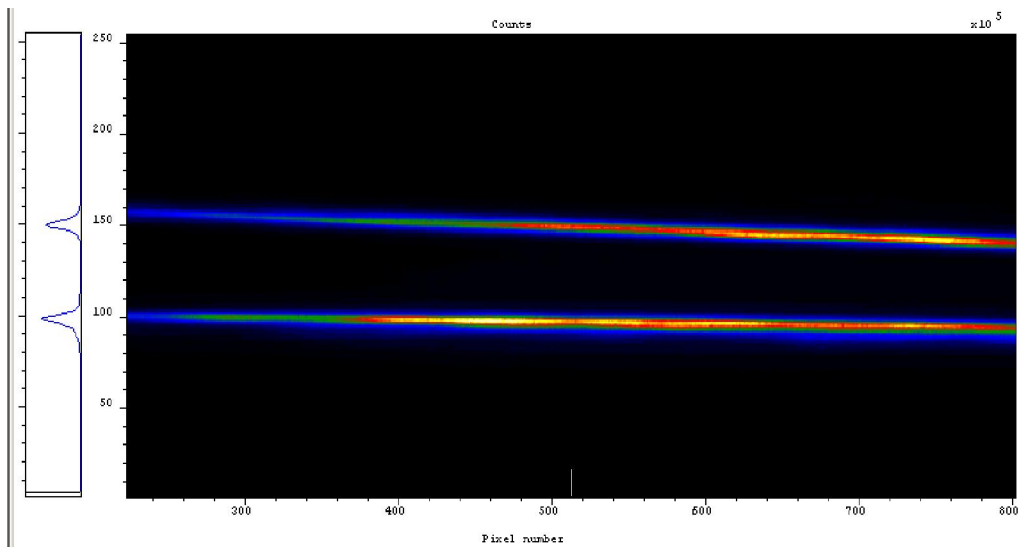


Figure 3.12. ICCD chip image showing the two separate areas illuminated by the signal and the background beam..

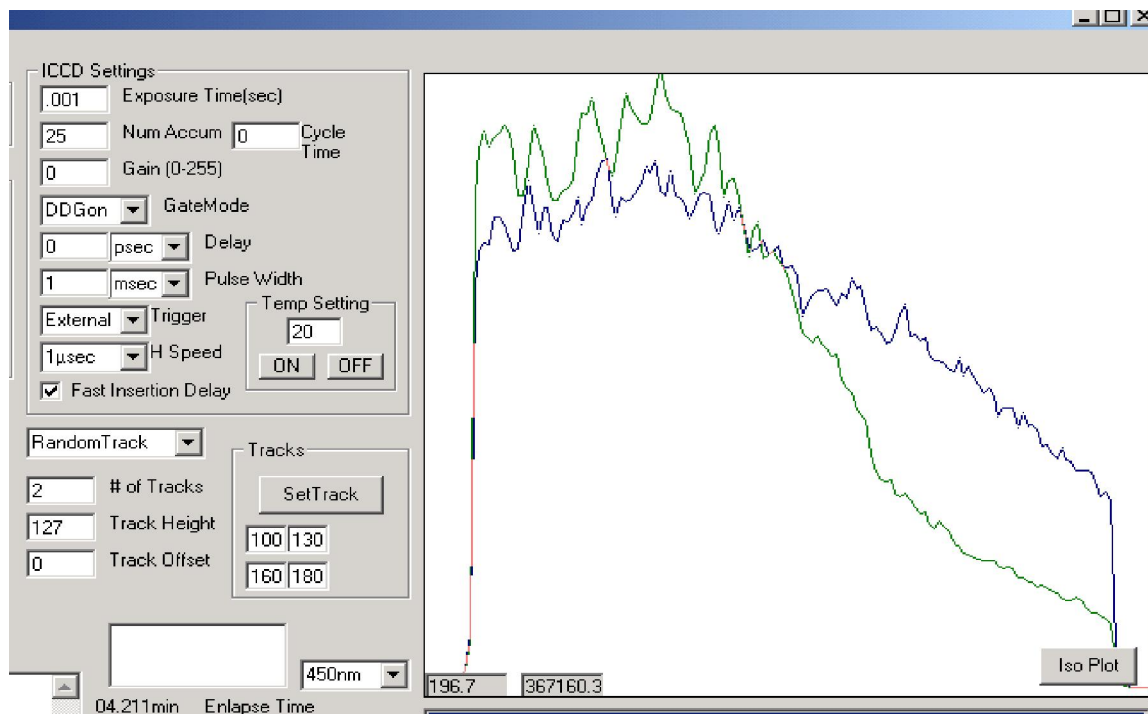


Figure 3.13. Software graph window view while acquiring data with the two-beam setup. It has two random tracks and each track is 30 pixels high.

any acquisition. This allows the user to adjust one beam vs the other by moving a neutral density filter in the beam path. To generate the correct absorbance spectra, both beams needed to be similar in intensity and form before loading the sample on the cell holder. When the cell was secured on the cell holder a small difference between the two beams was recorded, corresponding to the light absorbed by the sample. To verify the system, the instant absorbance spectra was determined and compared to the one obtained in a steady state UV-Vis spectrometer.

3.4. Results goal 6

A vast amount of data was acquired during each experiment, so it was impossible to analyzed each spectrum individually. Roughly, a normal experiment with 128 delay positions using the random-track option, with only two areas and 20 repetitions per position, produced 2,500 spectra; or more than 3 million data points. Hence a global fitting technique was used to analyze the data. Global fitting techniques build on the principle of standard nonlinear least square fitting (LSF). It is used to approximate multiple fits simultaneously, and it is based on the concept of sharing parameters across fits. The singular value deconvolution (SVD) method was based on a linear algebra principle that states that for any $M \times N$ matrix \mathbf{A} , where M (rows) is higher or equal to the number N (columns), it can be written as a product of three matrices \mathbf{U} , \mathbf{W} and \mathbf{V} . The first matrix is an $M \times N$ column orthogonal matrix, the second matrix \mathbf{W} is an $N \times N$ diagonal matrix and matrix \mathbf{V} is the transpose of an $N \times N$ orthogonal matrix. (20)

$$[A] = [U][W][V^T]$$

To use the SVD analysis a software tool was created in LabView[®] using the graphical programming virtual instrument tools (Figure 3.14). The LabView[®] package comes with the routines to apply the SVD analysis. The acquired data in text format is transferred to the LabView[®] virtual instrument (VI) for analyses. The VI output produced three matrices ready for further analysis. The created software has the ability of plotting the data in a 3D representation to provide a general overview of the data surface before mathematical analysis.

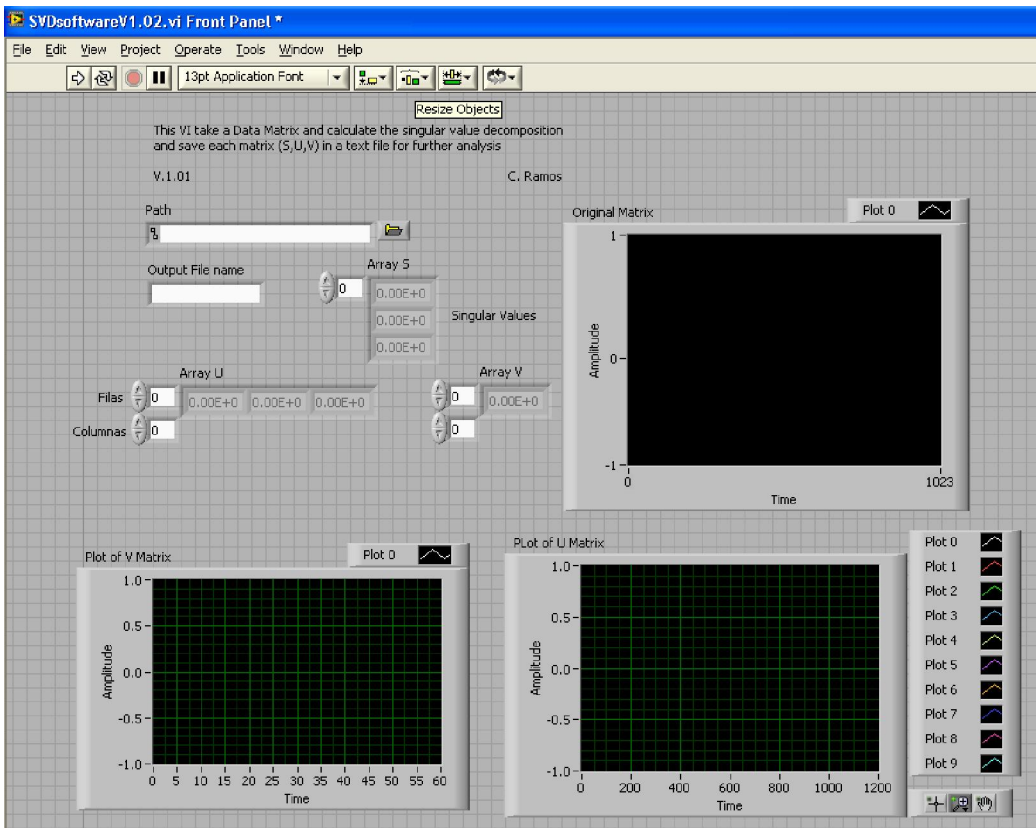


Figure 3.14. User interface of the virtual instrument created in Labview for data SVD data analysis. The input of the software is the text file with the intensity matrix, and the output will be three files with each deconvoluted matrix

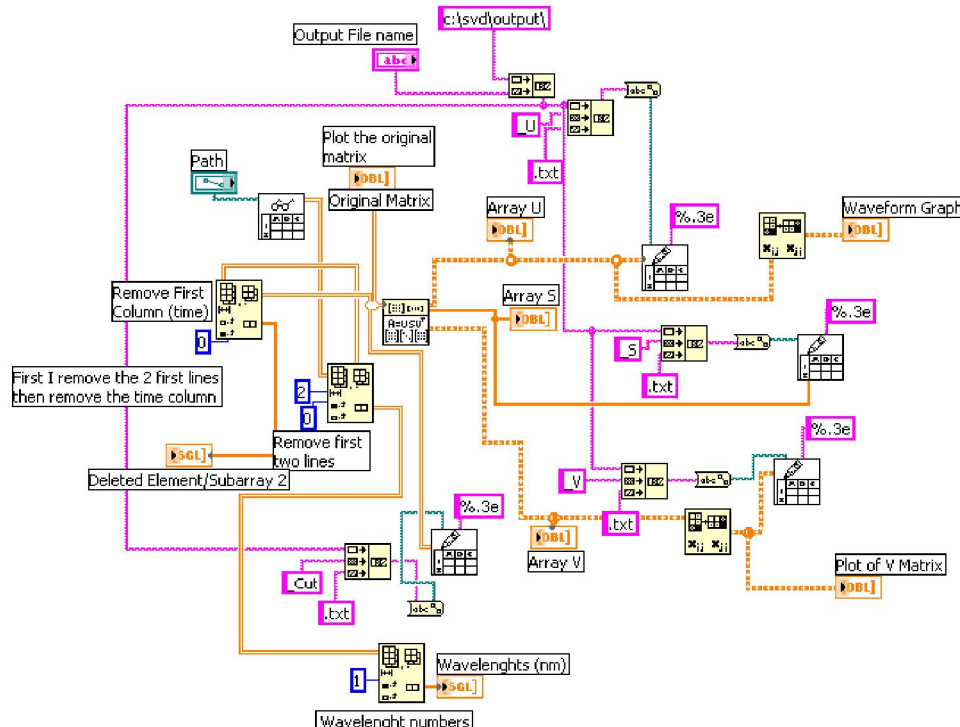


Figure 3.15. Graphic LabView® programming of the SVD analysis VI tool.

When the data is recorded with the acquisition software it is exported as a text file (.txt).

This file is an intensity matrix where each column represents a different delay position (time) and each row has the intensity at a specific wavelength.

t/λ	t_1	t_2	t_3	...	t_n
λ_1	I_{11}	I_{12}	I_{13}	...	I_{1n}
λ_2	I_{21}	I_{22}	I_{23}	...	I_{2n}
:	:	:	:	:	:
λ_m	I_{m1}	I_{m2}	I_{m3}	...	I_{mn}

Figure 3.16. Intensity matrix

The SVD tool is applied to this intensity matrix **[A]** and it is deconvoluted into three matrices, the first one is the $M \times N$ matrix which dependents on wavelength **[U]**, the second one has the singular values of the decomposition diagonalized matrix **[W]** and the third matrix is the time dependant $N \times N$ matrix **[V]**. Matrix **[U]** generates the absorption spectra of the species involved in the photo excitation process. The second matrix (matrix **[W]**) shows a list, in descending order, of numbers that will show the “weight” of each component. The higher the numerical value of the number in that list, the higher the contribution from that component to the overall data. Each of the other two matrices would be organized in descending order of contribution, column wise. If only the first three components summarize the total contribution to the analyzed data, the first three columns of the matrix **[U]** and **[V]** would be used for fitting and identification of the involved species. Using this method it is possible to “reduce” the

data to a few maximum components that usually can range from one to three. The third matrix, **V**, was dependent on time, indicating that each column will be the transient absorption kinetic (time vs. intensity) of the respective transient absorption spectra of matrix **U** (wavelength vs intensity). After the SVD analysis the transient absorption spectra were analyzed by comparing them with the steady state UV-Vis spectra of the complex under study, or with a combination of states (e.g. deoxy minus oxy, H₂S complex minus metaquo, etc). To plot the kinetic trace of that specific transient the specific column from the last matrix (Matrix V) was graphed. For the work done in Puerto Rico femtosecond laboratory that analysis was performed using Origin®.

Analysis of the data taken in France was conducted using a homemade software version (AVFOUR.exe) written by them. The was analyzed using their SVD analysis tool, also a homemade software, (SVD.exe), and the output from this software was transferred to another software (AVFOUR.exe) where the final fitting is performed. The fitting software has various capabilities and parameters that could be controlled to calculate the best fit to the data. For example, it can fit the data with a nonlinear time axis. In this respect, the measurements were conducted in various step windows since the data was acquired over a long time scale (from -50 fs to 500 ps). Specifically three time-windows were used during the experiment. The first one measures short time intervals (e.g. 0.5 ps), the second section longer time intervals (e.g. 50 ps) and the last section at even larger intervals (e.g. 100 ps). In this approach a total of 100 delay positions were evaluated, compromising a wide time range axis to study. Nonetheless, this allowed the analysis from from a few femtoseconds to hundreds of picoseconds.

Data acquired at the Ecole Politechnique, Paris France:

During the “practicum” at Paris France three complexes and three mutants were measured using their laser system setup. After each run, the data was analysed using a homemade software for SVD analysis. The data for the three complexes indicates the transient absorption for each sample and then the first SVD components of the matrix **[U]**, as a function of wavelength. The selection of those principal components was based on the singular values (matrix **[W]**) obtain for each sample. Each sample was measured several times and the data consisted of the various spectra between the photo-excited sample and the un-excited sample.

3.5. Results goal 7

This section summarizes the preliminary validation of the ultrafast system setup designed and constructed in the Chemistry Department at the University of Puerto Rico at Mayaguez; as well as the data acquired during the “practicum” at the Ecole Politechnique in Paris Palassau France.

Puerto Rico Laser System:

During the setup and development of the system, various measurements were performed to verify the system stability and to test the developed software and tools. Figure 3.17 shows a screen shot of the software. The stability of the signal was measured with only 50 accumulations per scan, a rather average value for such experiments. The experiment noise analyses (Figure 3.18) for the setup was below the 0.2% range within scans (blue trace).

Practicum experiments

Figure 3.19 shows the first SVD kinetic decay component for the three rHbl samples. The orange trace corresponds to the rHbl ferrous (Fe^{II}) sample, the blue trace to the rHbl ferric (Fe^{III}) sample and the pink trace to the rHbl Ferric H_2S ($\text{Fe}^{III}\text{-SH}_2$) complex. Also Table 3.3 summarizes the mathematical fit analyses for the three complexes. For simplicity, the kinetic traces of the second and third SVD components are not included in this figure.

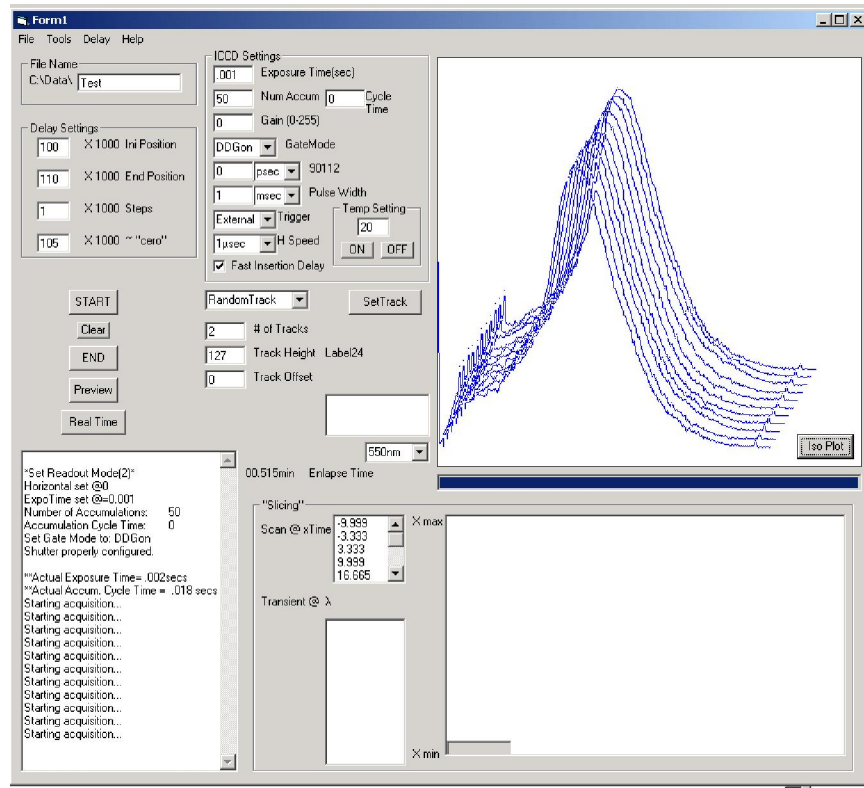


Figure 3.17. Screen shot of the developed program running with rHb sample for stability test. Notice that only 50 accumulation where taken per scan.

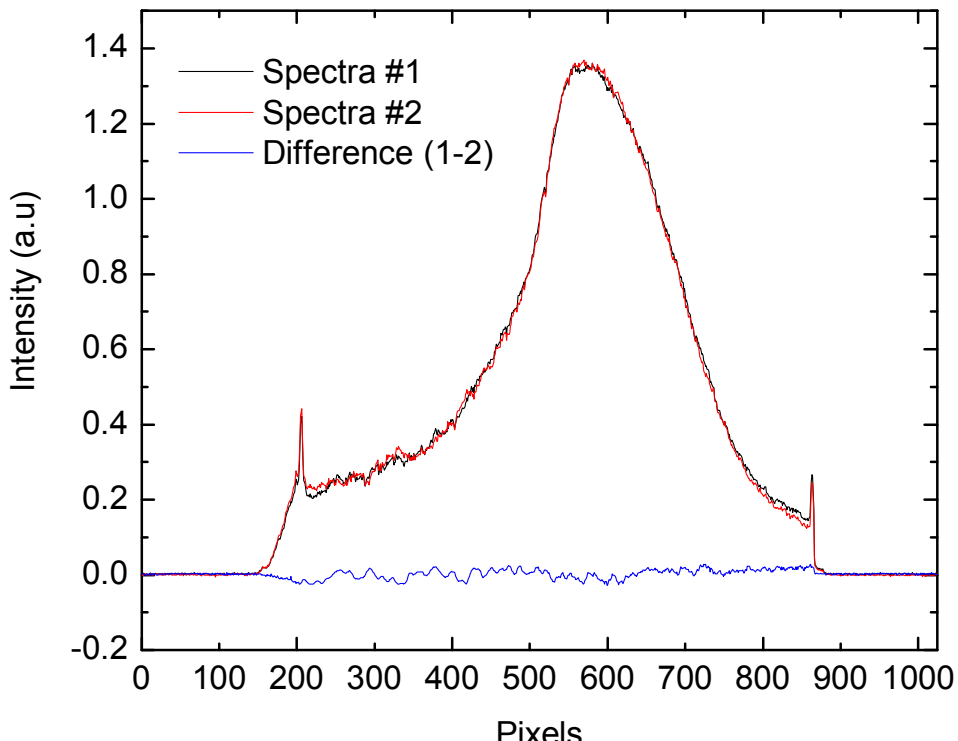


Figure 3.18. Absorption spectra of two consecutive delay positions without pump (red and black). On Blue the difference between the two.

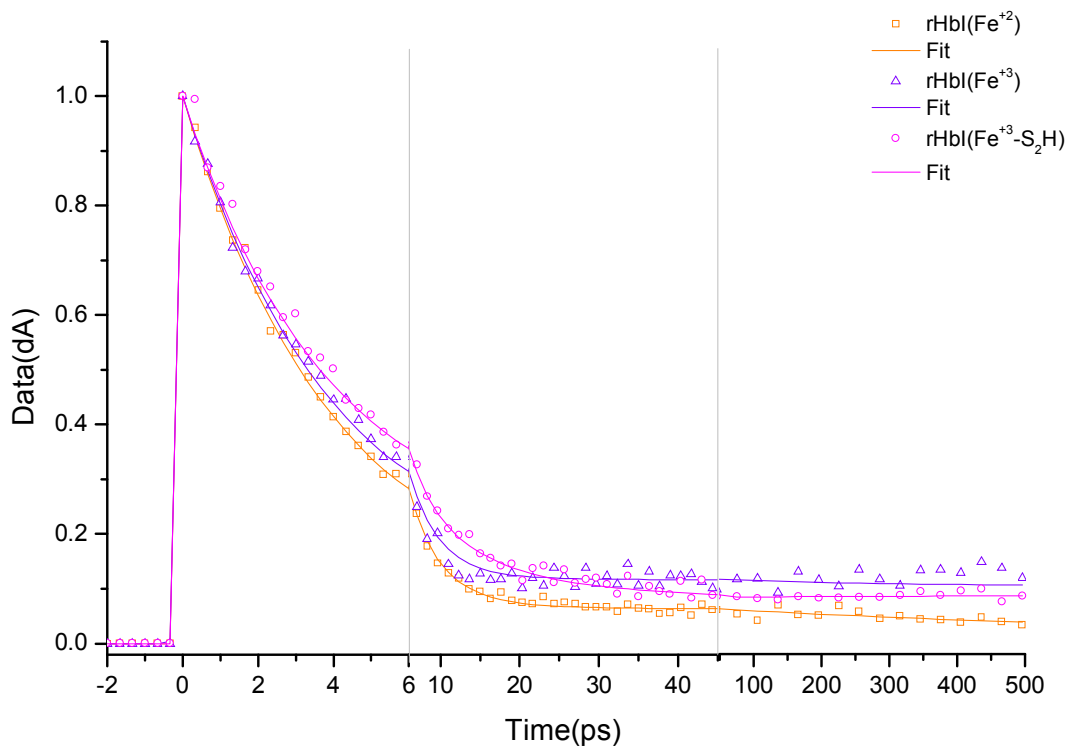


Figure 3.19. Kinetic traces of the first SVD component for the recombinant Hbl protein with the different oxidation states. (Fe^{+2} , Fe^{+3} , $\text{Fe}^{+3}\text{-S}_2\text{H}$)

File Name	OxState	τ_1	$A_1 (\%)$	τ_2	$A_2(\%)$	C
hb27089v	Fe^{+2}	3.8	91	6.4	3	6.5
hb25089u	Fe^{+3}	3.8	87			13
hb26089u	$\text{Fe}^{+3}\text{H}_2\text{S}$	3.4	50	12	40	10

Table 3.3. Kinetic Fit values for the first SVD component for each complex.

3.5.1. Ferrous sample (Fe^{II})

The rHbI ferrous (Fe^{II}) species was the first analyzed. The sample was prepared as stated on the material and methods section prior to laser exposure. The stability of the sample was monitored using a UV-Vis spectroscopy before and after laser exposure. Figure 3.20 shows the transient absorption of the rHbI sample during a short interval time scale ($\leq 10\text{ps}$). As shown in the figure, there is no major wavelength displacement; that is, the intensity of both peaks moves toward the zero intensity line over time. There seems to be an expansion (red shift) and contraction (blue shift) over time of the curves, visible in the right and left side of the traces. The data was plotted over a longer time scale ($\leq 50.0\text{ps}$) (Figure 3.21); and it shows that after $\sim 14.0\text{ ps}$, the transient absorption and the bleaching signal almost disappeared. A displacement of the isosbestic point after $\sim 14\text{ ps}$ was also observed.

The data was analyzed by SVD to deconvoluted it into the most significant components. The first three component numerical values are shown in Table 3.4, representing the “weight” of each component. Each of the traces in Figure 3.22 were multiplied by their respective singular values to have a visual correlation of the contribution from each component. The major contribution comes from the first component (value=0.3400). The trace shows a bleaching signal at 429nm and an induced absorption at 446nm (black trace). The second SVD component (value =0.943); (red trace) presents a smaller profile when compared to the first component and it showed a negative absorption band at 439nm and a positive absorption band at 407 nm. The third component (value=0.291) (green trace) is almost unnoticeable and was therefore discarded.

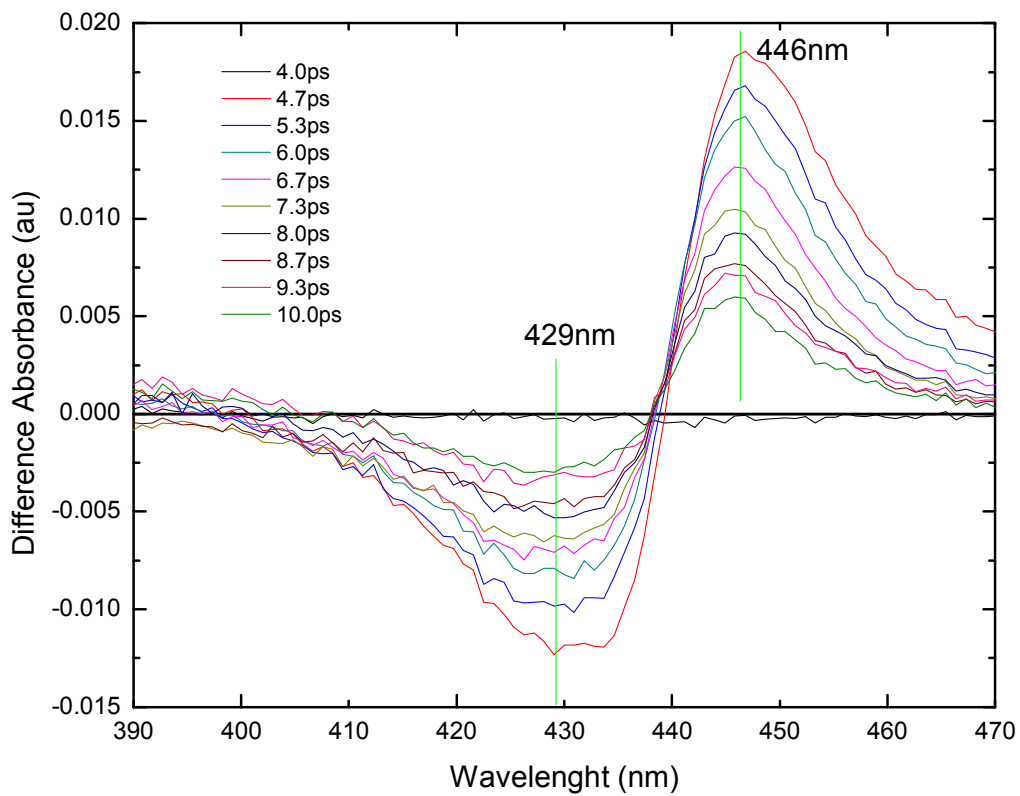


Figure 3.20. Difference transient absorptions at various delay positions (4-10ps) of the ferrous (Fe^{II}) rHbl sample

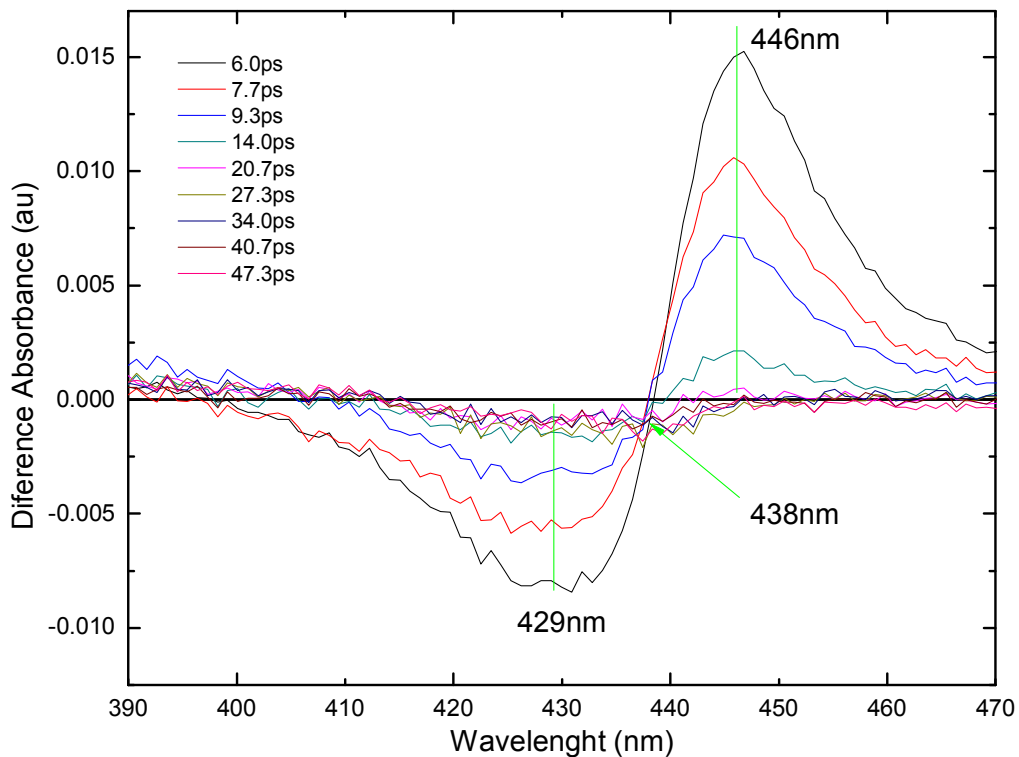


Figure 3.21. Difference transient absorption at various delay positions (4-47 ps) of the ferrous (Fe^{II}) rHbl sample.

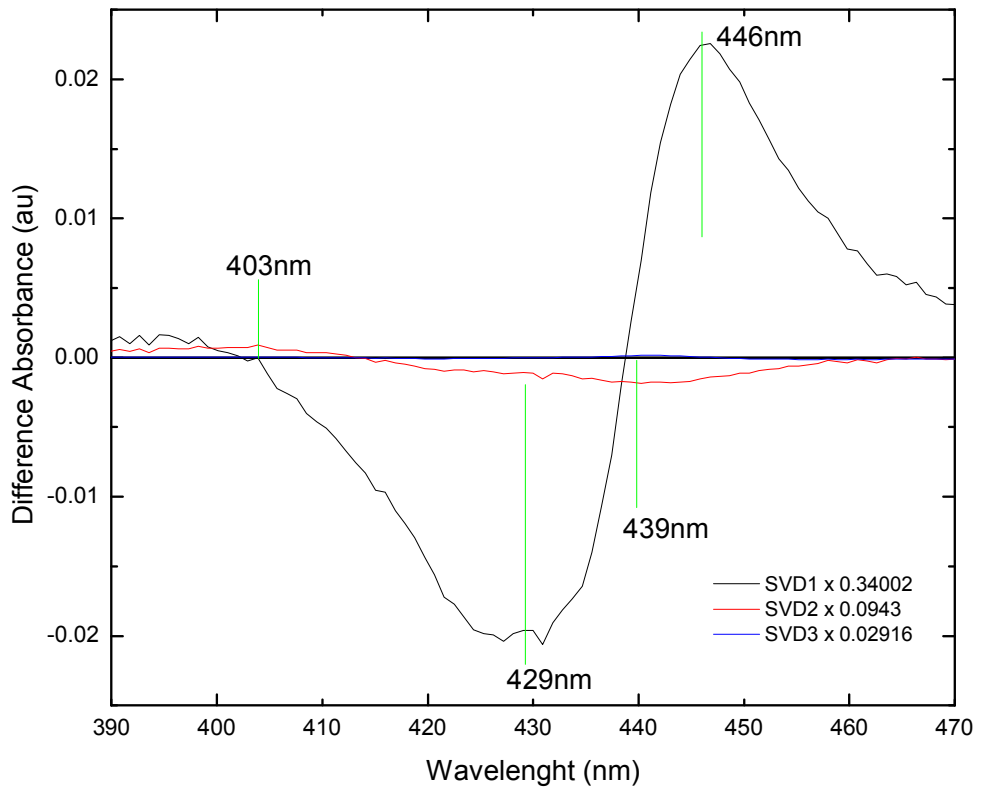


Figure 3.22. First 3 SVD transient absorption components for the ferrous (Fe^{II}) rHbl sample each multiply by their respective singular values.

Component	Singular Value
1	0.3400
2	0.0943
3	0.0291

Table 3.4. Singular Values for the SVD analysis of the ferrous rHbl data.

3.5.2. Ferric Wt Hbl (Fe^{III})

Figure 3.23 shows various transients at various delay positions ranging from 4.6 ps to 10 ps (short time scale) for the ferric (Fe^{III}) rHbl sample. Over time there was no displacement of either the metaquo bleaching signal or the induced absorption band. When the data was evaluated over longer time scales (from 4.33 to 47ps) (Figure 3.24) the 432 nm band was displaced to 417 nm and the 405 nm to 412 nm. This displacement occurred after ~10 ps. Figure 3.25 show the first three components of the SVD analysis for the metaquo species. Each spectrum was multiplied by its singular value (Table 3.5) to have a better view of the contribution of each component. The major contribution arises from the first SVD component (value=0.2300) but there was a small, but possible significant contribution from the second component (value=0.0738). This second trace shows two bands one at 417 m and the other at 437 nm.

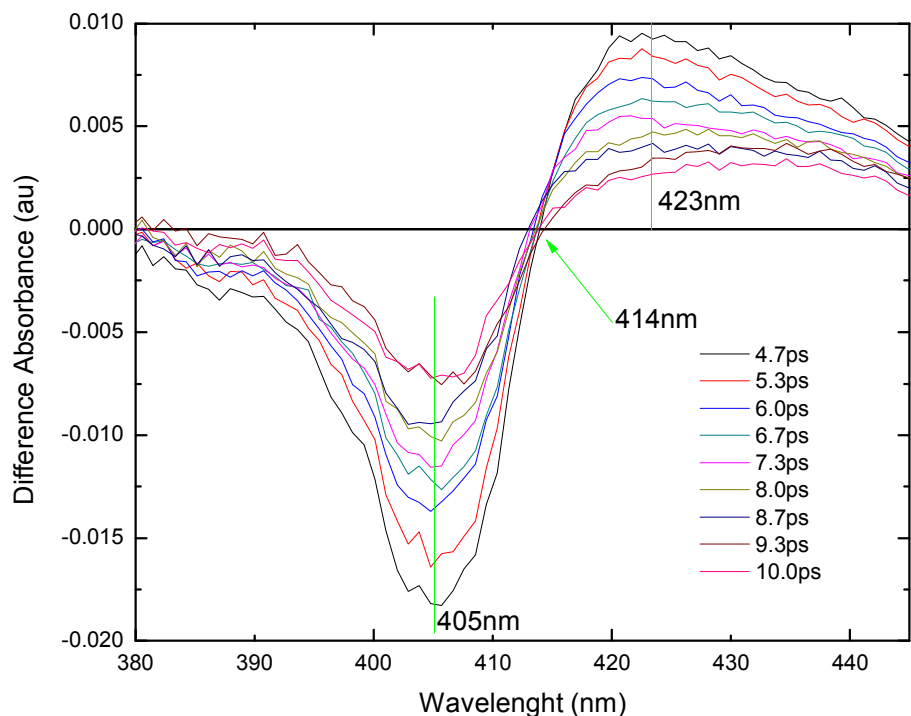


Figure 3.23. Difference transient spectra of the ferric (Fe^{III}) rHbl sample at various delay positions. (Short time scale)

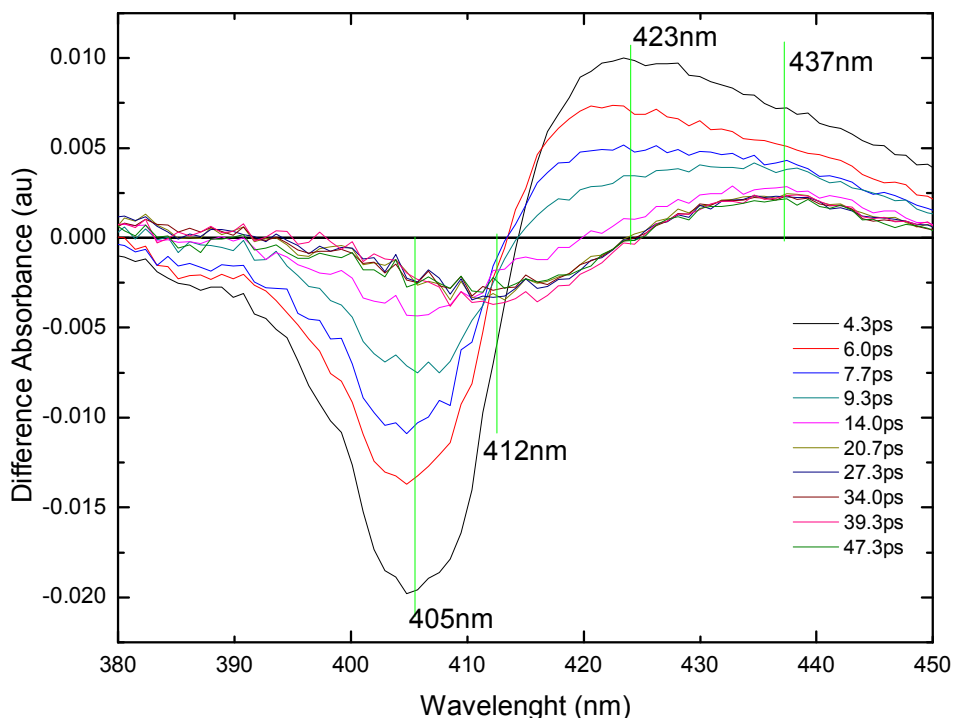


Figure 3.24. Difference transient spectra of the ferric (Fe^{III}) rHbl sample at various delay position. (Long time scale)

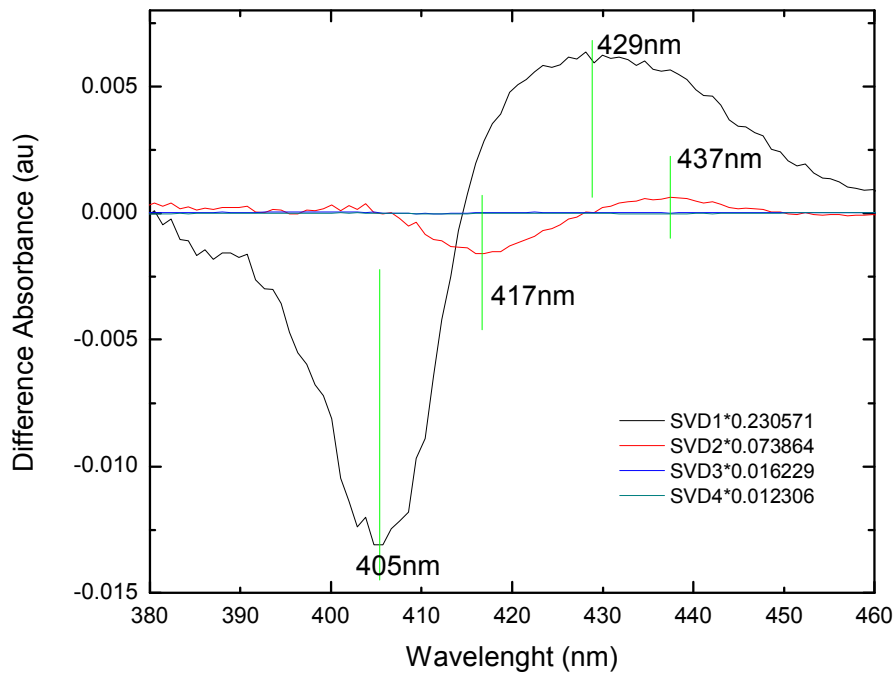


Figure3.25. First 4 SVD components of the ferric (Fe^{III}) sample multiply by its respective singular value

Component	Singular Value
1	0.2306
2	0.0738
3	0.0162
4	0.0123

Table 3.5. Singular Values for the SVD analysis of the ferrous rHbI data.

3.5.3. Ferric Wt HbI H₂S (Fe^{III})

For the hydrogen sulfite (H₂S) rHbI complex, similar measurements were performed. A plot of various transient over short time scales is shown in Figure 3.26. This plot shows that the right side absorption band experienced a blue shift as time evolved. The maximum moved from 447 nm to 444 nm while the left side absorption band (at 395 nm) did not move and it only showed a change in intensity as a function of time. The band at 424 nm (HbI-H₂S) simultaneously moved toward zero intensity as time evolved. As similar behavior was observed over longer time scales (Figure 3.27), but the traces moved closer to zero intensity as time evolved. Figure 3.28 shows the first three SVD components of the SVD analysis for the ferric-H₂S sample. Each trace was multiplied by their respective singular value (Table 3.6). The major contribution came from the first component (value=0.2232) trace, but there was some structure of the second and third components.

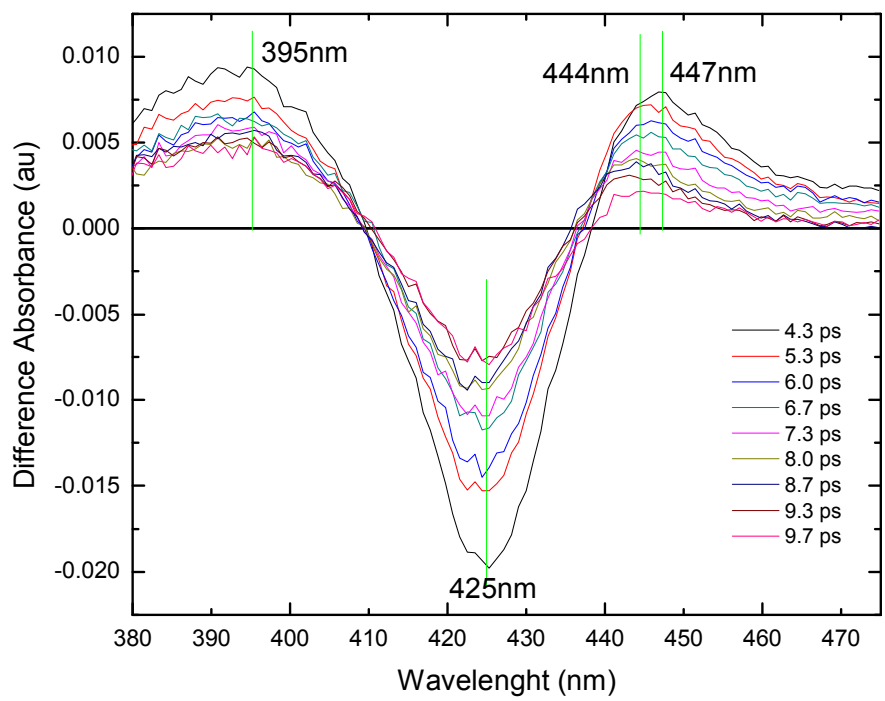


Figure 3.26. Transient spectra of the ferric- H_2S rHbl sample at short time scale.

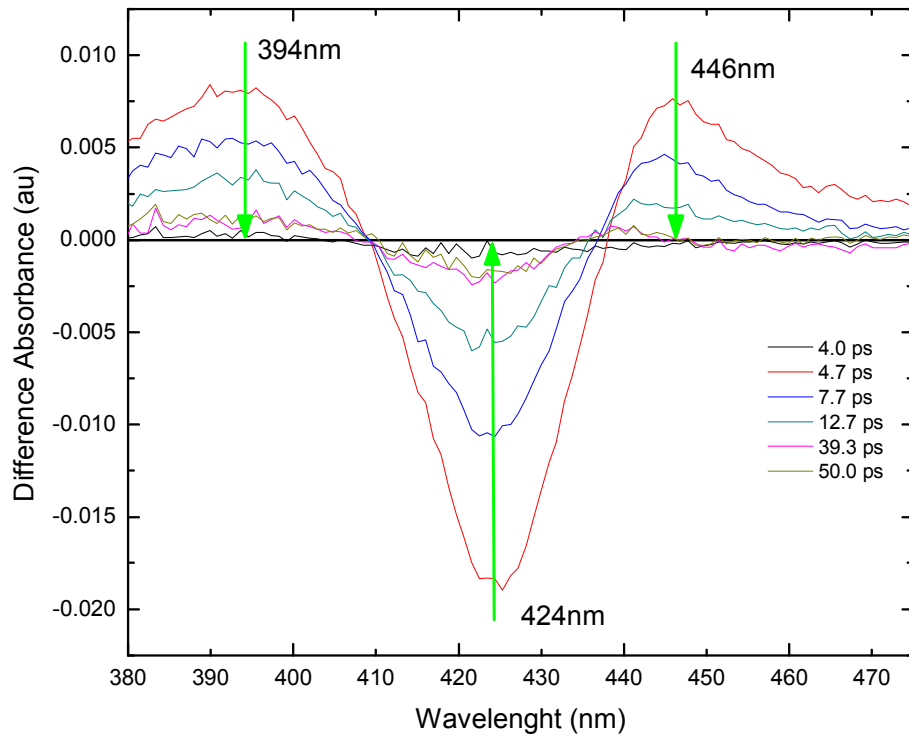


Figure 3.27. Transient spectra of the ferric- H_2S rHbl sample at long time scale.

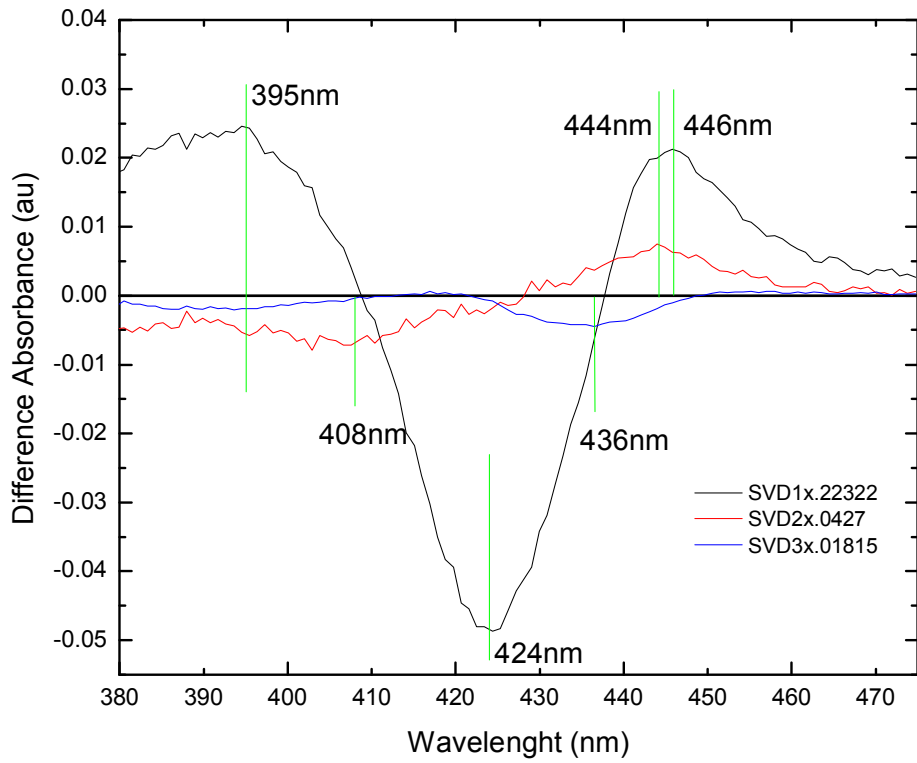


Figure 3.28. First three SVD components for the Ferric-H₂S rHbl sample multiply with their respective singular value.

Component	Singular Value
1	0.2232
2	0.0427
3	0.0181

Table 3.6. Singular Values for the SVD analysis of the ferrous rHbl data.

3.5.4. Fe^{II}-NO (Fe^{II})

The next figures (Figure 3.29) show the data for the Fe^{II}-NO sample. Figure 3.29 show the transient absorption of the first 10.0 ps. A bleaching signal was observed at 418 nm and an induce absorption signal at 439 nm. The curve resembled a classical ligated-to-unligated evolution of the reaction. Figure 3.30 shows the first three SVD component of the rHbl-NO analyses. The major contribution comes from the first component although there was some structure of the second and third components.

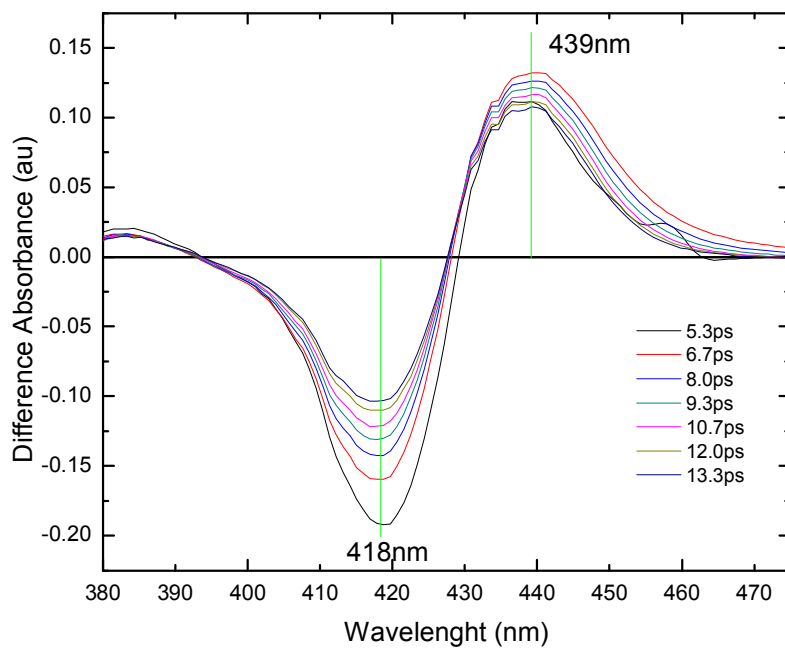


Figure 3.29. Transient absorption of rHbI-Fe^{II} NO reduce with ascorbate at different delay positions.

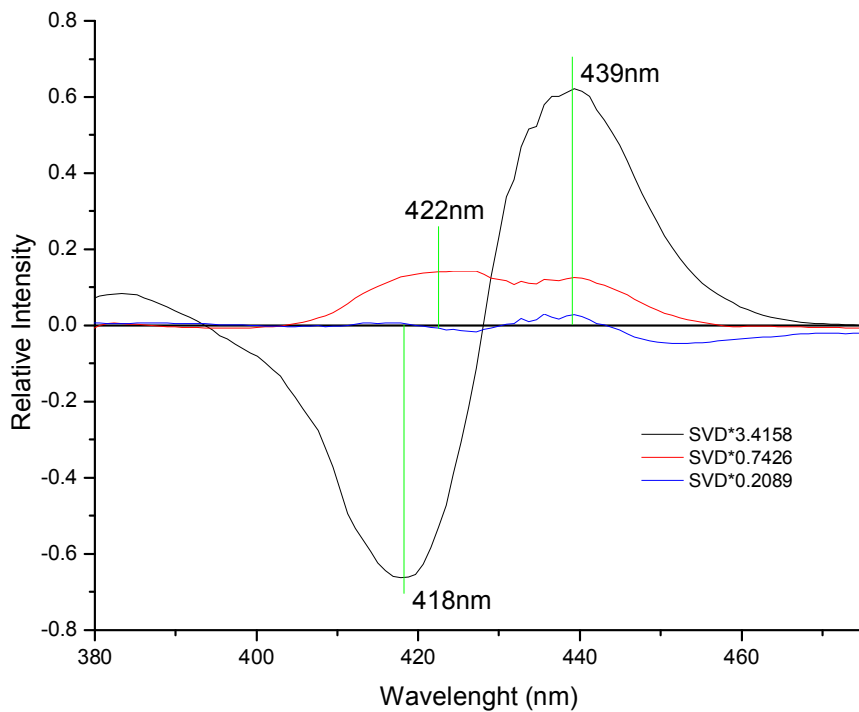


Figure 3.30 First three SVD components for the rHbI-Fe^{II}NO sample. Each trace was multiply by their respective singular value.

4. Discussion:

4.1. Ferrous rHbI sample (Fe^{II})

Before analyzing the transient kinetic data, the transient absorption spectra were analyzed to evaluate the species involved after photo-excitation of the samples. When the first SVD transient absorption spectrum was compared with the steady state (ss) spectrum of the ferrous sample, the bleaching signal at 429 nm (inverted difference spectra) corresponded to the classical Soret band of the deoxy specie (~435 nm) (Figure 4.1). The positive induced absorption was assigned to an excited state absorption and/or the vibrational cooling of the photo-excited ground state. The isosbestic point for this sample was located at about 439 nm. To illustrate trace displacement, a normalized plot of the transient absorption was generated (Figure 4.2). There was no significant displacement of the 446 nm maxima and 429 nm minima bands. There was an expansion and contraction over time of the traces, visible on the right and left side of the plots characteristic of the vibrational cooling of a hot heme (28). The insert on the shows only a minor movement of the isosbestic point (~1nm), which can be attributed to the inherent experimental error in the measurements. At longer time delays (Figure 4.4), there was a large shift of the isosbestic point from 439 nm to 445 nm. This displacement of the signal suggested that at least two processes were taking place. The first one, is assigned to the photo-excitation of the ferrous rHbI; that resulted in a vibrational excited state (with a time constant of 3.4 ps); while the second one is attributed to the disappearance of the Fe^{II} rHbI after the end of the excited-state cooling. From the SVD component plot (Figure 4.3), the major contribution comes from the first component which shows a bleaching signal at 429 nm and a positive transient

absorption at 446 nm. This SVD component was similar to the transient absorption recorded at 1 ps. The second SVD component was smaller and showed a bleaching centered at 439 nm and a broad induced absorption at ~398 nm. A signal around 395-400 nm corresponded to a 5-coordinated ferric heme. We assigned the induced absorption of the second SVD to the appearance of a ferric heme due to immediate photo-oxidation with time constant of 6.4 ps and 300 ± 20 ps.

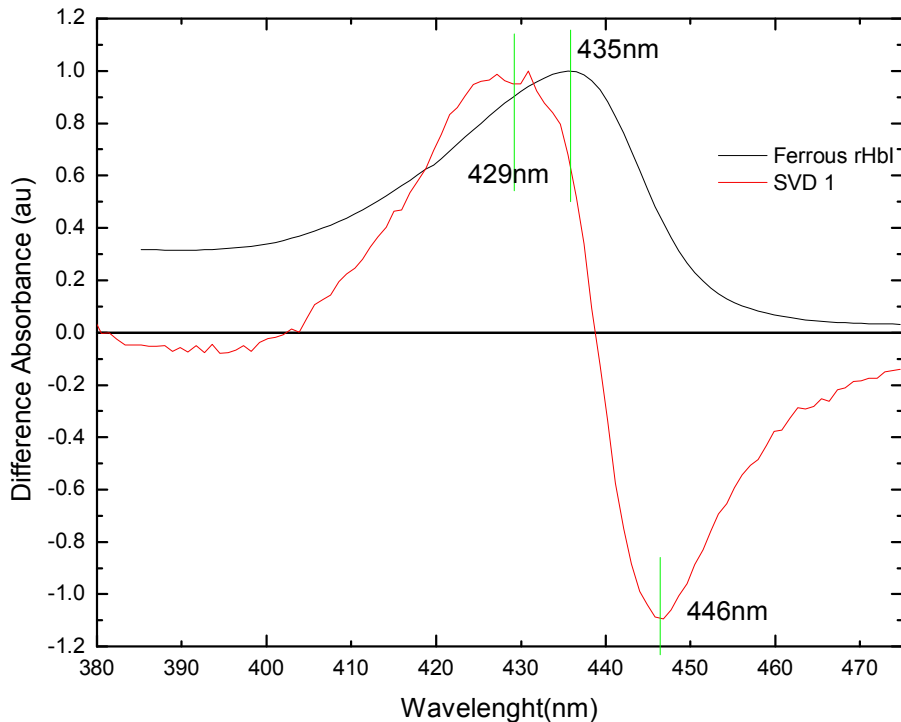


Figure 4.1. Comparison between the first SVD component for the ferrous rHb(Fe^{II}) sample with the steady state UV-Vis spectrum of the same sample.

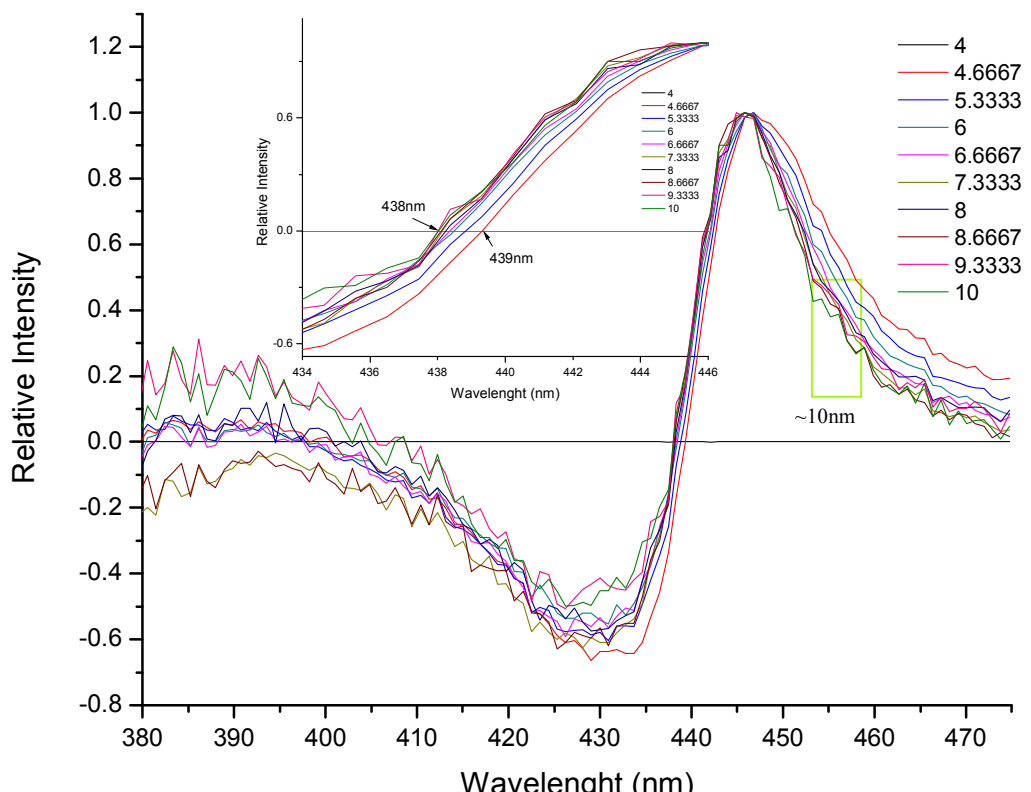


Figure 4.2. Normalize data of the ferrous (Fe^{II}) rHbI sample to show the blue shift of the induce absorption signal (4ps is the flat black line). The insert show the isobestic region for the same plot.

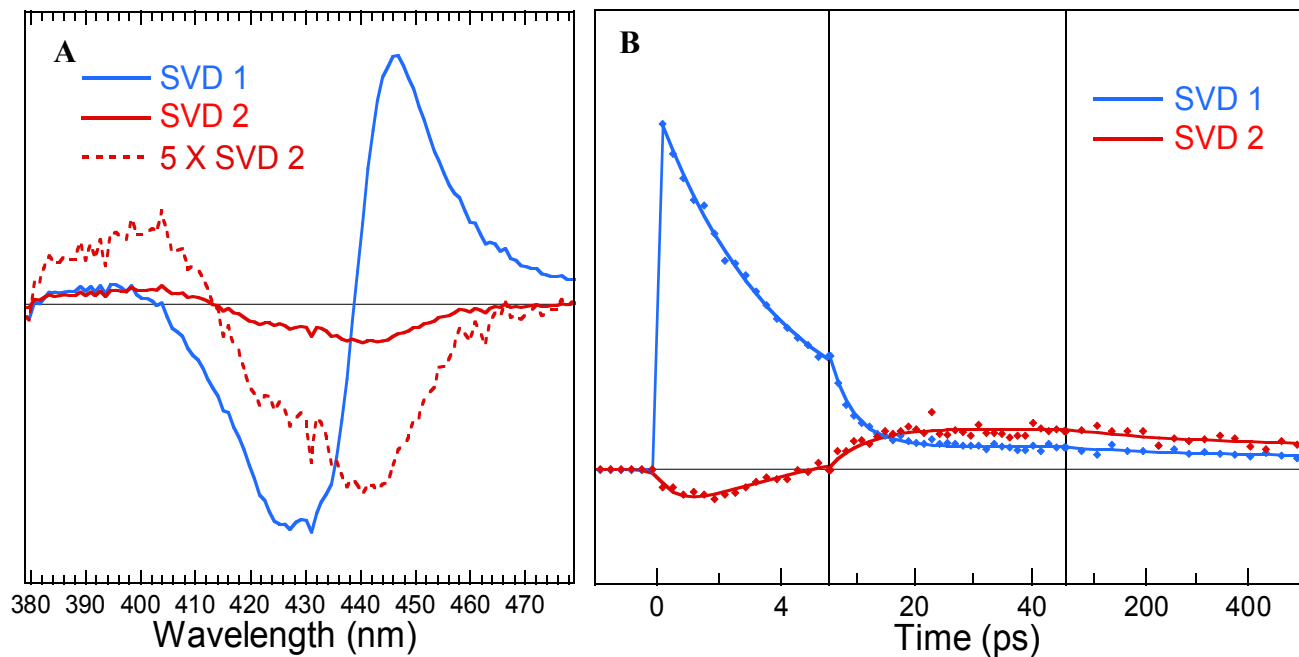


Figure 4.3. Panel A show the first 2 SVD components for the Ferrous rHbI sample. The dotted red line is the second SVD multiply by a factor of 5. Panel B show the corresponding kinetic traces for the two SVD.

4.2. Ferric rHbI sample (Fe^{III})

The ferric rHbI sample, also known as metaquo, showed a different spectrum compared to the previously discussed ferrous complex. When the first SVD component was compared to the UV-Vis steady state spectra, the 405nm band corresponded to the classical metaquo species ($\lambda_{\text{max}} = 407 \text{ nm}$) (Figure 4.4). The positive part of the difference spectra was attributed to the formation of some excited states of the photo-excited ferric heme. A comparison plot was made between the first SVD component and the difference spectra obtained when we subtract the ferric rHbI metaquo (ss) specie (Fe^{III}) to the ferrous rHbI (ss) (Fe^{II}) sample (Figure 4.4). The negative signal for the two traces corresponded to the metaquo species. On the positive side, the maximum for the SVD component was $\sim 426 \text{ nm}$ while that of the deoxy specie was at 434 nm. Based on this trace, we can rule out the formation of a heme deoxy species after the photo-excitation of the ferric rHbI sample. The transient absorption spectrum shows that there was no displacement, neither of the metaquo bleaching signal, nor the transient absorption band on this time scale. A normalized version of the transient absorption spectra was prepared (Figure 4.5) on this plot and showed that there was a considerable displacement of the signal at 423 nm after 8.0 ps. The signal moves from 423 to 432 nm while the signal corresponding to the metaquo specie (406 nm) remained relatively constant. At longer time scales ($\sim 50.0 \text{ ps}$), there was a displacement of both bands, from 423 nm to 437 nm and from 405 nm to 412 nm. The initial bleaching after the photo-excitation at 406nm was readily assigned to the disappearance of the ferric heme ground state. Since there was no induced absorption at 395 nm, the water molecule presumably does not photo-detach after excitation; like in the case of ferric

myoglobin (28). The decrease of the initial induced absorption band revealed the appearance of a second induced absorption band centered at 437 nm, with a bleaching at 417 nm. Therefore, at least two processes occurred after the photo-excitation of the ferric Hbl, leading to an apparent shift of the transient spectra. From the SVD analysis plot, the major contribution comes from the first SVD component but there was a small but maybe significant contribution from the second component. This component comprised an induced absorption band whose time constant, $\tau=3.8$ ps, representing the major decay component (Table 3.3). This decay constant was assigned to the heme vibrational excited states relaxation. This second trace showed two bands one at 417 nm and the other at 437 nm. We compare this trace with the different steady state spectra for the ferric rHbl minus ferrous rHbl and oxy rHbl minus ferrous rHbl samples (Figure 4.6). The second SVD trace looked more similar to the oxy minus deoxy species although there was considerable displacement between the wavelengths. The similarities of these difference spectra indicate that a small amount of Hbl-O₂ was present in the sample.

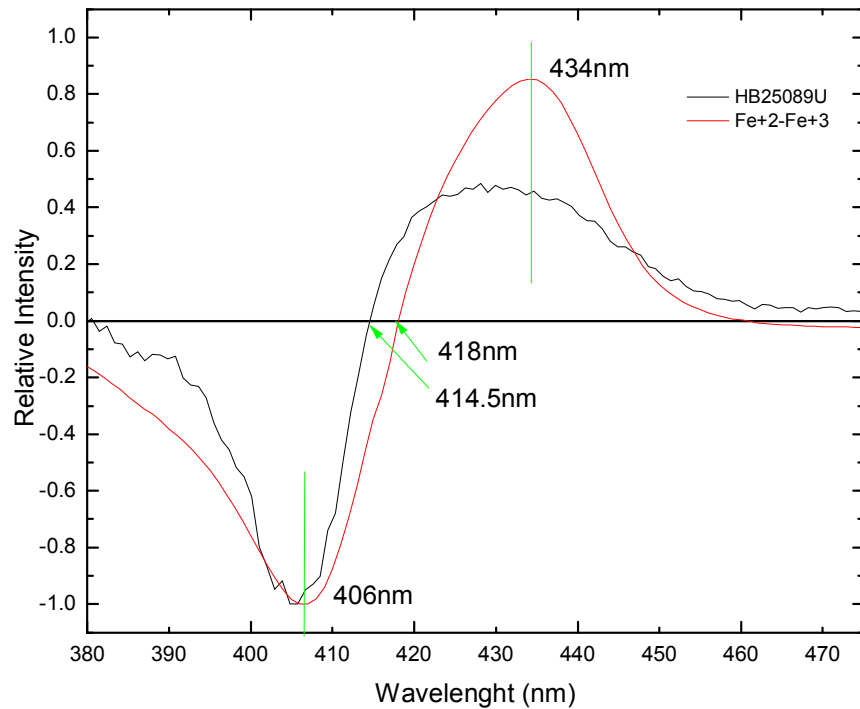


Figure 4.4. Normalized (negative) data comparison between the first SVD component of the Fe^{III} sample and the ferrous (Fe^{II}) minus ferric (Fe^{III}) steady state spectra.

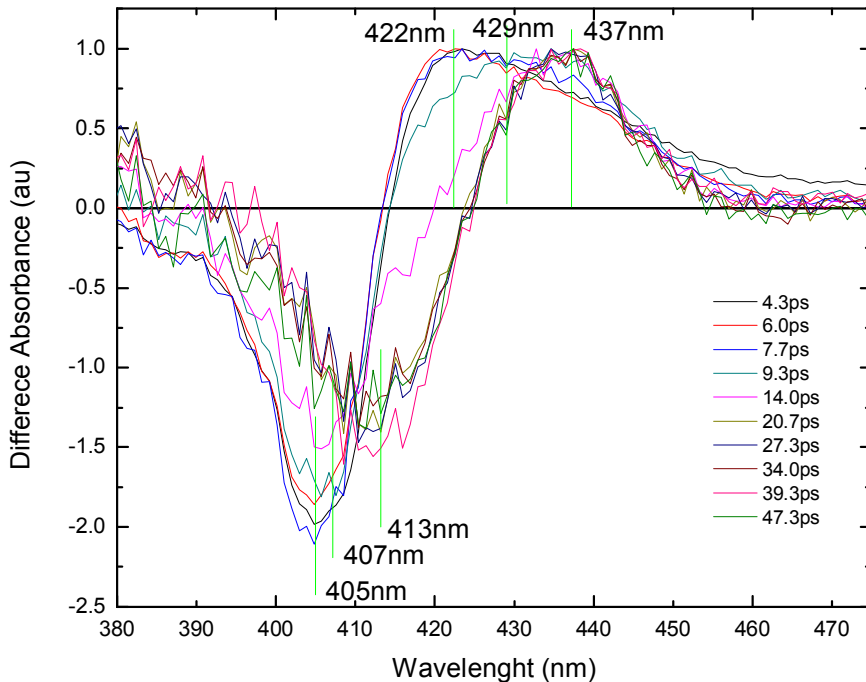


Figure 4.5. Normalized data from the rHbl Fe^{III} sample at long time scales. The first “group” at 422nm corresponded to 4.3-7.7ps. The green and pink traces corresponded to 9.3 and 14.0 ps.. There was a red shift with time on both signals (bleached and induced absorption).

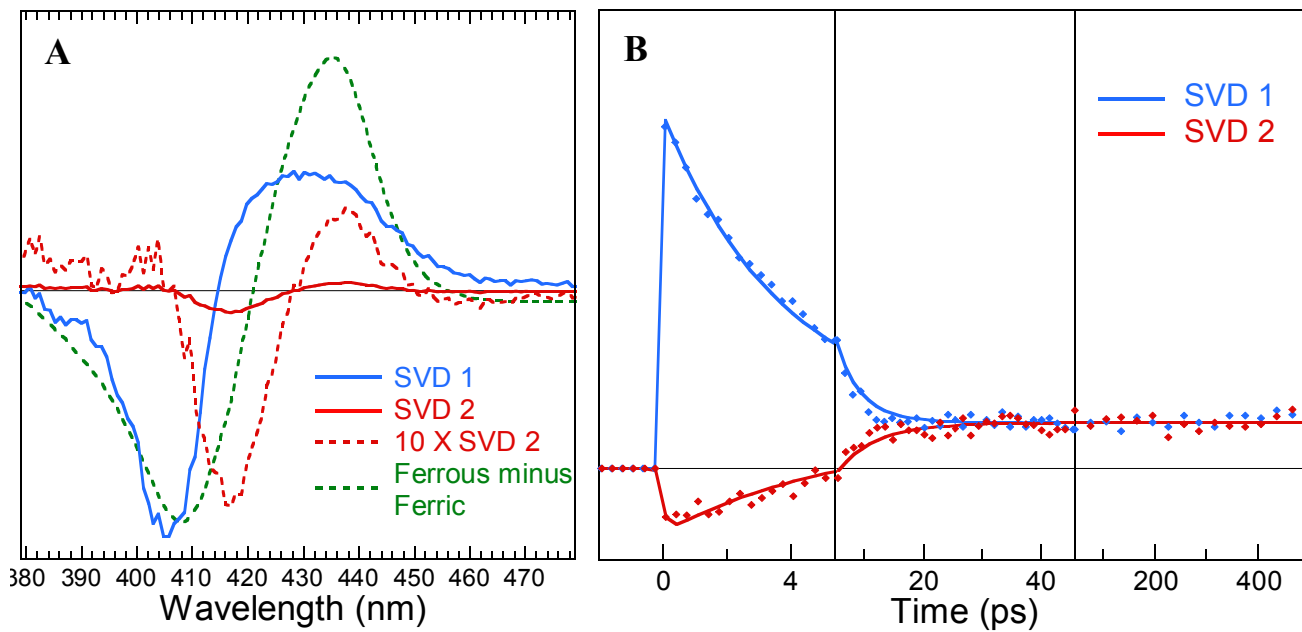


Figure 4.6. Panel A show the first 2 SVD components of the ferric rHbI sample. The red dotted trace is the second SVD component multiply by a factor of 10. Panel B show the kinetic traces of the two signals.

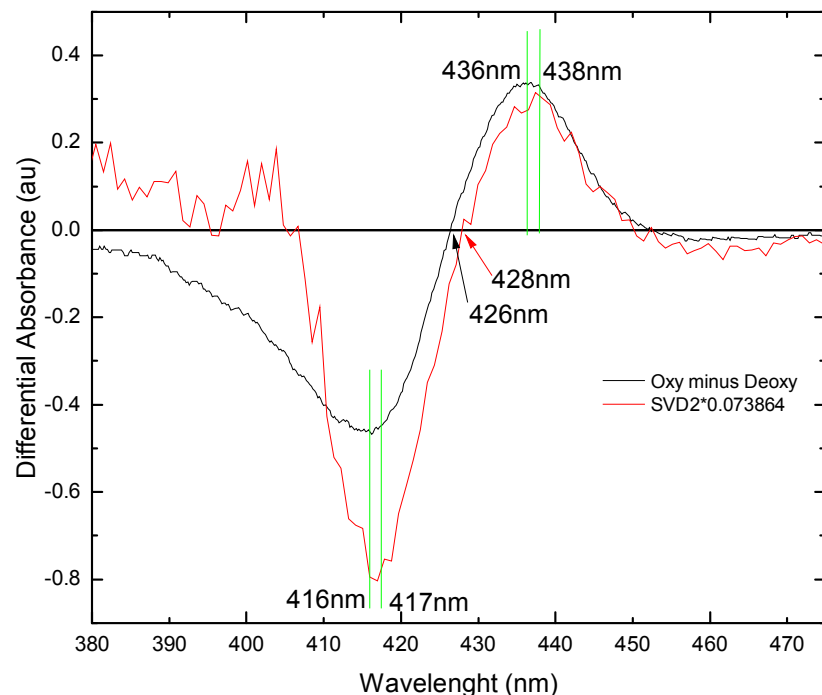


Figure 4.7. Comparison between the Oxy minus deoxy Fe^{II} rHbI sample and the SVD2 component of the Fe^{II} sample analysis. (SVD component was multiply by its singular value)

4.3. Ferric H₂S-rHbI sample (Fe^{III}-H₂S)

Figure 4.8 shows the comparison between the transient absorption of the ferric-H₂S rHbI sample with the steady-state difference spectra, between the ferric-H₂S rHbI and the ferric rHbI sample. The spectra are different indicating that we are not dealing with a simple ligated-to-unligated species evolution. The steady-state difference spectra shows an absorption band at 407 nm, corresponding to the ferric rHbI sample and a bleaching signal at 429 nm, corresponding to the ferric-H₂S rHbI maxima. The transient absorption shows a single bleaching at 424 nm and two induced absorption signals at 397 and 445 nm. The bleaching signal is readily assigned to the disappearance of the ground state liganded species whose steady state Soret band was located at 426 nm (Figure 4.8). A plot of various transients at different delay positions is shown in Figure 4.9; in this plot, the right side absorption band experienced a blue shift as time evolved. The maximum apparently moved from 447 nm to 444 nm, while the left side absorption band (at 395 nm) did not move. It only showed a change in intensity as a function of time. The band at 424nm (HbI-H₂S) simultaneously moved toward zero intensity. To illustrate this displacement, a normalized version of this plot was generated. This plot demonstrates that the 447 nm band exhibits a blue shift with time and after ~9.0 ps, it shifts to 444 nm. Similar behavior was observed at longer time scales (Figure 4.9. A normalized version of that plot was constructed, (not shown), and again there was a displacement of the 446 nm band while the other two bands remained almost identical. An SVD analysis (Figure 4.10) was performed but the technique could not untangle the contribution from the different species. The analysis was then performed by plotting and fitting the kinetics at specific wavelengths for the three signals (Figure 4.11). From the

mathematical fits at the specific wavelengths we obtained only two exponential components with similar time constants indicating the presence of only two processes. The first one ($\tau = 3.4 \pm 0.5$ ps) similar to what we found previously for the ferric and ferrous rHbI samples, was assigned to the vibrational relaxation of the heme. The second one ($\tau = 12 \pm 1$ ps) was assigned to the geminate recombination of the photo-detached H₂S. The induced absorption band at ~395 nm was assigned to the 5-coordinated ferric heme vibrationally excited electronic ground state, based on other heme protein analyses (28).

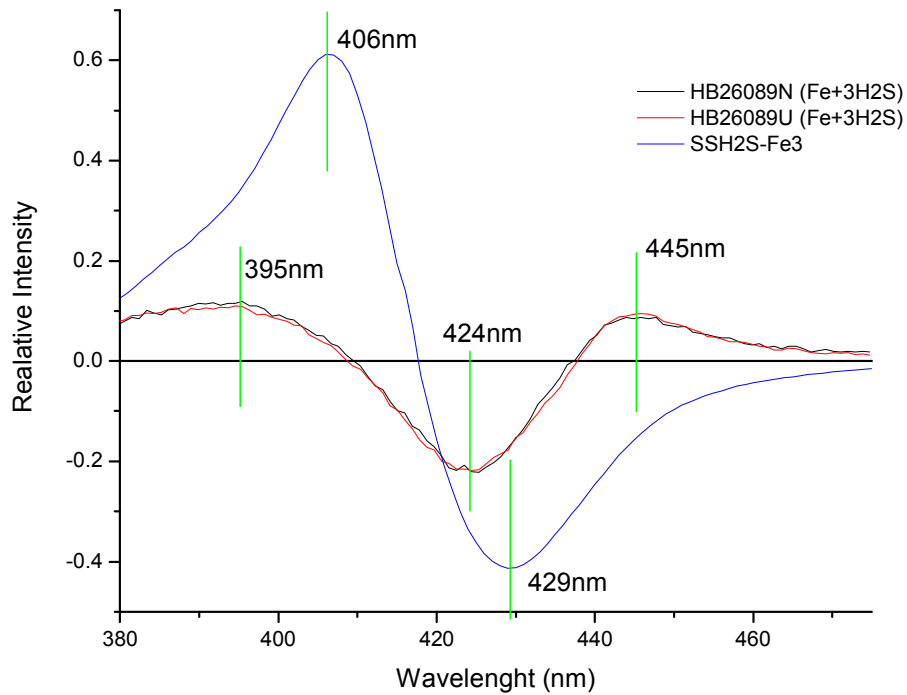


Figure 4.8. Comparison between the SVD-I component of the ferric-H₂S sample and the steady state difference spectra between the ferric-H₂S and the ferric sample

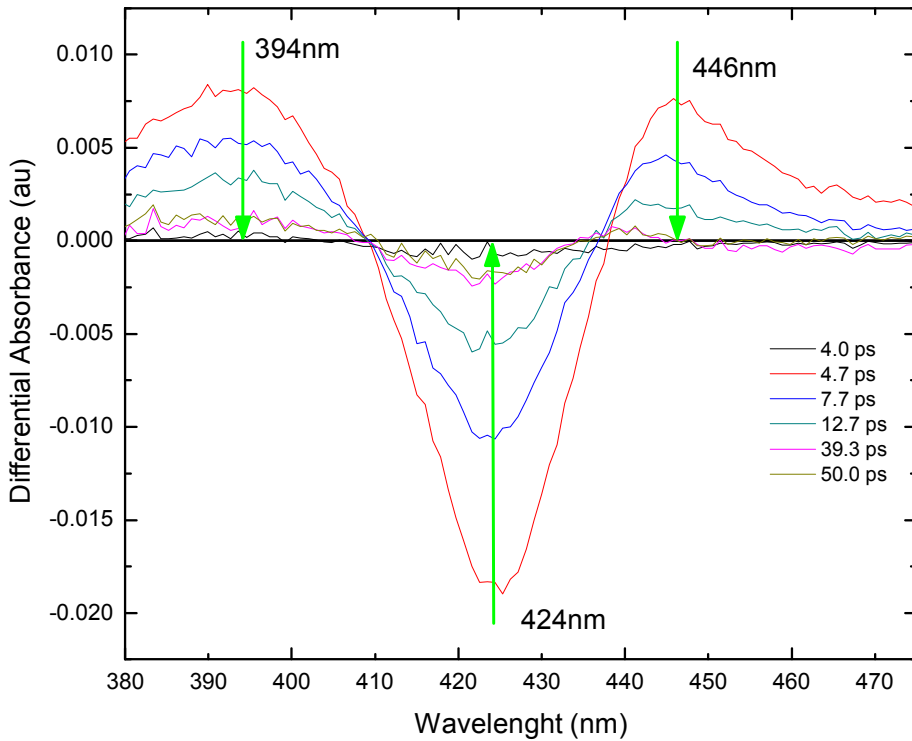


Figure 4.9. Transient spectra of the ferric-H₂S sample at long time scale.

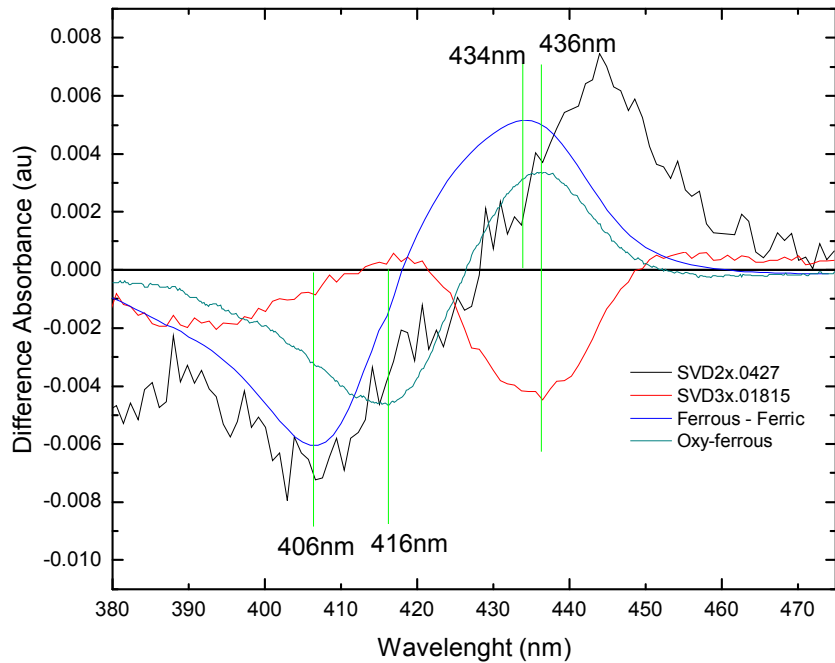


Figure 4.10. SVD 1 and SVD2 of the Ferric-H₂S sample compared with the heme (ferrous minus ferric) and (Oxy minus ferrous) steady state spectra.

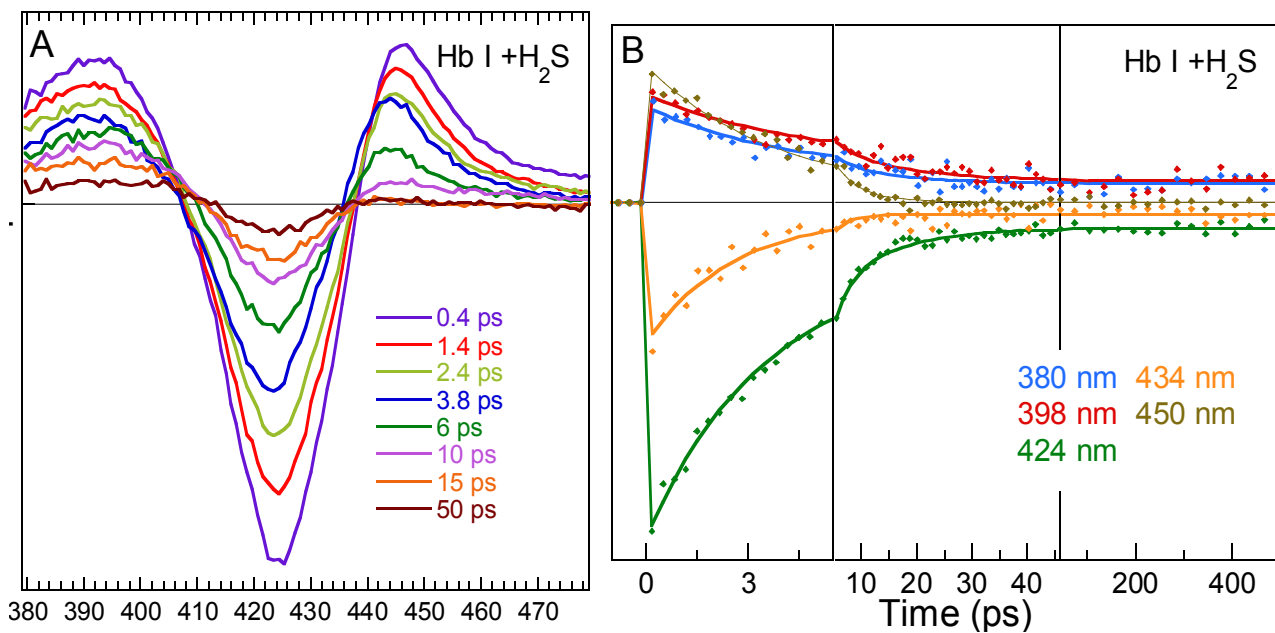


Figure 4.11. Panel A show transient absorption signals for the rHbI-H₂S sample at different delay position. Panel B show the kinetic traces at various wavelengths for the rHbI H₂S sample

Based on the ultrafast H₂S experiments and other experiments performed in our group (22) we concluded that the H₂S sample does not follow simple ligated-to-unligated species evolution spectra. We deduced from the data that there should be at least three species involved in the photoexcitation of the H₂S complex. On Figure 4.12, we compare the fourth transient absorption for the fourth species discussed in this study, with the transient absorption curve (blue line) for rHbl-H₂S presenting a bleaching signal with two “wings” one at 446 nm and another at 395 nm. None of the other three samples showed this similar trend, instead the other samples showed a derivative-like trace. A model plot was constructed using the normalized steady-state spectra from the ferric (Fe^{III}), H₂S(Fe^{III}-H₂S) and ferrous (Fe^{II}) rHbl samples (Figure 4.13). Each trace on this figure was generated by making a difference spectrum between a mathematically “sum of species” contribution and the rHbl-H₂S normalized spectra. This mathematical sum of species was generated by adding the product of each sample spectra times a factor coefficient, so that the end result was equal to “one” (example: $.2Fe^{+3} + .4H_2S + .2Fe^{+2} = 1$ spectra). The factor coefficient must be a number between 0 and 1 and the sum of the three factors must equal to one. The plot demonstrated that as the contribution of the rHbl Fe^{II} species is increased (from .06 to .80) the contribution of rHbl Fe^{III} is decreased (from .47 to .10). The curve takes a similar shape to the one obtained in the ultrafast transient absorption experiments. Because all three involved species were mathematically related, as one of the species contributions was reduced the other changed, because the mathematical sum was normalized to one. If contribution of the rHbl-Fe^{II} was reduced, we had to increase the contribution from the rHbl-H₂S, the rHbl-Fe^{III}, or both. Based on this we performed two steady-state models

one in which we fixed the contribution of the rHbl-H₂S specie (to .2H₂S) and changed the other two. If the contribution of Fe^{II} was reduced (from .6 to .4)

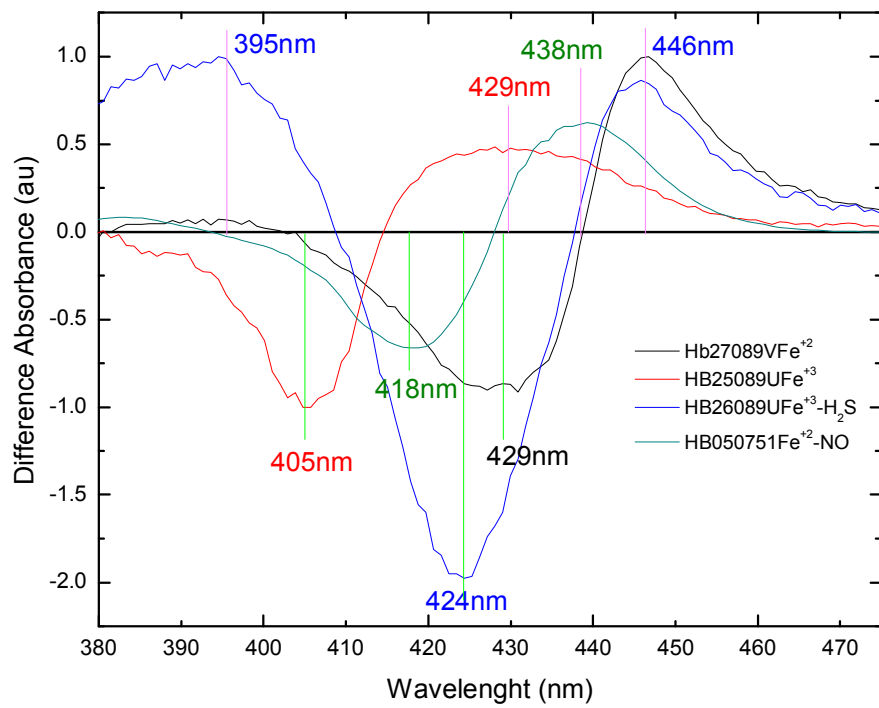


Figure 4.12 First SVD transient component for the 4 different samples (3 new 1 old).

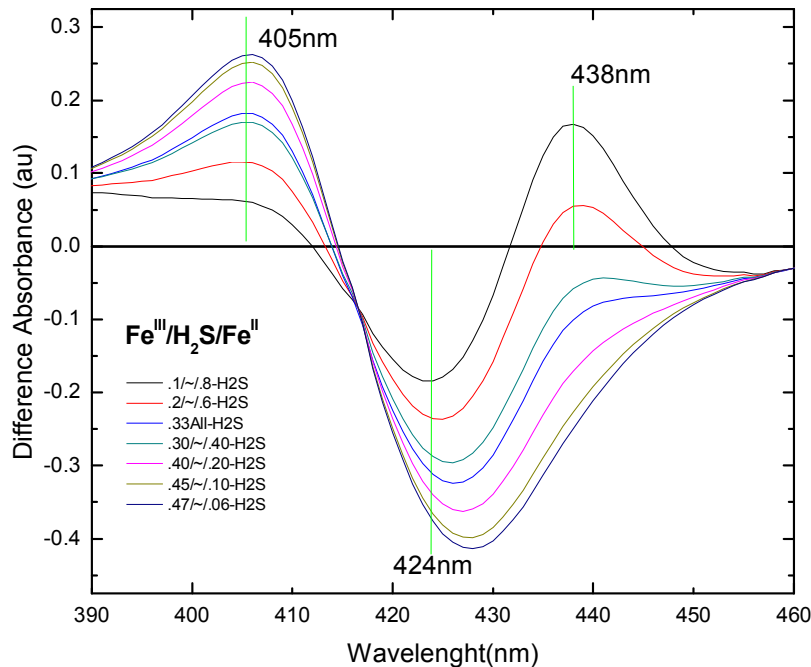


Figure 4.13. Steady state normalized modeling difference spectra of a ration combination of the Fe^{III} , H_2S and Fe^{II} species against the H_2S spectra.

and the contribution of rHbl-Fe^{III} (from .20 to .40) was increased, the intensity of the ~400 nm region band increases and the ~440 nm region band decreases. If we tried the opposite (increase the contribution of Fe^{II} and reduce the contribution of Fe^{III}) the inverted trend is observed (red trace on Figure 4.13). Although this steady state mathematical representation involved only the sample ground state, there were certain similarities we could observe. Associating this model to the ultrafast transient absorption spectra we could deduce that the induced absorption band at 446 nm was affected more if the concentration of ferrous (Fe^{II}) rHbl specie change, while the 395nm induced absorption band was affected as a function of a ferric rHbl (Fe^{III}) concentration change. From all the model traces generated (Figure 4.13) the one that looked more similar to the ultrafast transient absorption data was the one where the contribution followed this ratio $.2\{\text{Fe}^{+3}\} / .2\{\text{H}_2\text{S}\} / .6\{\text{Fe}^{+2}\}$. The discrepancies between the induced absorption “wing” bands λ_{\max} could be attributed to the model we were working which is in the ground state, ie the transient absorption had contribution from the excited states. If we tried another model combination (Figure 4.14) where the Fe^{II} species factor was fixed to .6 and change the contribution for the Fe^{III} and the rHbl-H₂S, a similar behavior was observed. This could be generalized so that there was a linear relationship between the Fe^{III} contribution and the ~400nm region band so that as it increased the band increased in intensity while the ~440nm region band decreased.

As a preliminary experiment, when we compared the H₂S complex measurements for three different mutants, Figure 4.14, we saw that each one presented a very similar curve trace with some noticeable differences on the induced absorption signals. Otherwise the band corresponding

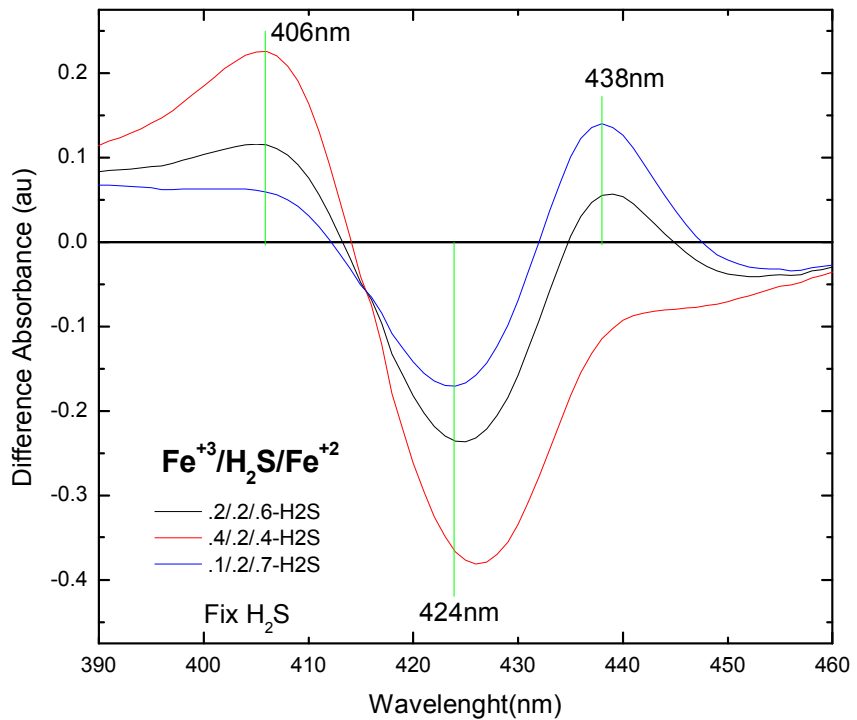


Figure 4.14. Normalize model steady state different spectra where the **rHbI-H₂S** contribution is constant and the other two changed.

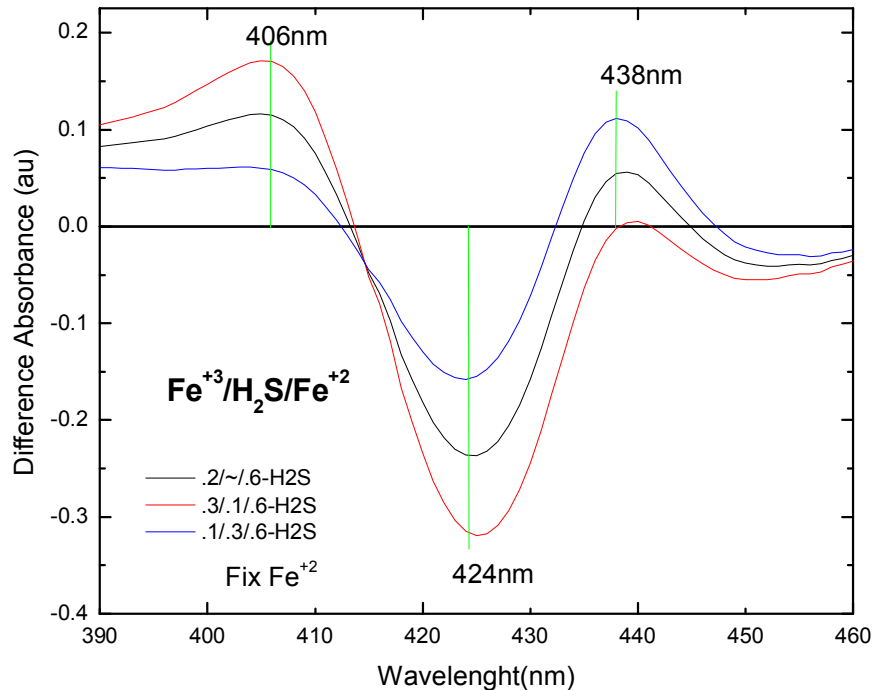


Figure 4.15 Normalize model steady state different spectra where the **rHb-Fe^{II}** contribution is constant and the other two changed

to the H₂S complex remains reasonably constant between the three samples. From this figure, the black trace corresponds to the rHbl-H₂S complex, two “wings” were almost balanced (the intensity for both induced absorption signals (395 and 446 nm) had a comparable intensity. The valine mutant (red trace) showed a higher intensity of the 446 nm band and a reduction of the 395 nm band. We can presume that the valine mutant presented a reduction of the Fe^{III} character and an increase on the Fe^{II} contribution. Data from Resonance Raman experiment of various H₂S mutants (22) showed that the H₂S complex exhibited a tendency toward reduction of the complex, apparently induced by the presence of H₂S. Each mutant exhibited certain relationships between the Raman markers for a Fe^{II} or Fe^{III} oxidation states (ν_3 and ν_4). For the GlnE7Val mutant complex with H₂S, the intensity of the 1374 cm⁻¹ was the highest, which was characteristic of a Fe^{III} oxidation state. Thus, we expected an increase of the contribution of the Fe^{III} signal (that could come from the contribution of the H₂S complex and from the metaquo species) which could translate into an increase of the ~400 nm band and a reduction of the 440 nm band. This behavior was the opposite of what we observed with the mutant traces.

The GlnE7His mutant H₂S complex (blue trace on Figure 4.13) had the opposite behavior from the GlnE7Val mutant. The blue trace indicates that the induced absorption band at 395 nm exhibited a higher intensity than the one at 446 nm. When we analyzed this behavior against the already published resonance Raman data (22), we can see that in the Raman experiments the histidine mutant showed a similar intensity for both Raman markers (ν_3 and ν_4). So we would expect a similar contribution from both oxidation states. Or when compared with the Raman data for the rHbl

sample, an increase of the Fe^{II} contribution should have translated based on our model to an increase of the ~440 nm band. Our model and the data showed an opposite behavior.

Based on this discussion, we can establish a simple three-model system to try to explain the transient absorption data obtained. It seemed that after photoexcitation at least two different states could be populated, one involving a Fe^{II} deoxy-like species and another involving a Fe^{III} metaqueo-like species.

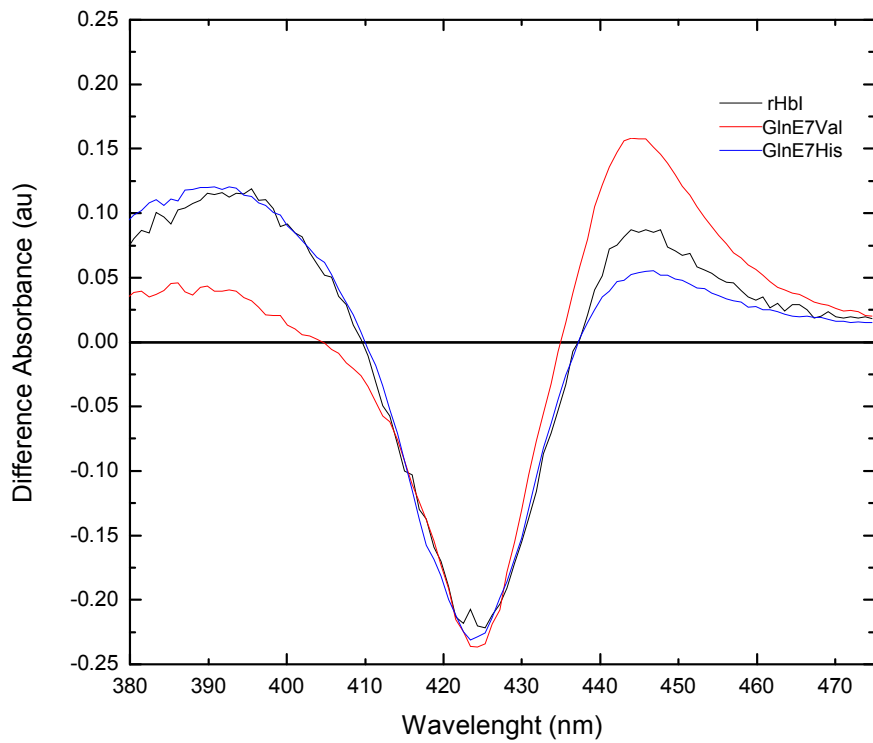


Figure 4.16 Comparison between the first SVD transient absorption spectra for three H₂S mutant complexes

5. Conclusions and future works

The ultrafast laser system setup acquired data of a wavelength region for a heme protein and a laser dye within the time frame of the laser repetition rate (~1KHz). We proved that the software acquired and handled the amount of data on that fast acquisition frame. The acquired data could be easily utilized to check preliminary data and analyses to draw quick decisions to determine if more data is needed.

The improved fermentation process proved to be of great help when large volumes of samples were needed. Also, from all the parameters changed the addition of Mg to the media was the key parameter for the ultra-high yield cell production. Regarding the rHbl experiment, we saw that the photo excitation of the H₂S complex did not show a classical ligated-to-unligated evolution. Based on the experiments performed we could say that there are at least three species involved. It is highly possible that one of those species was a deoxy-like species with a coordination of Fe^{II}. The preliminary mutant studies with H₂S showed some variations that were affected by the mutation. Other mutants needed to be analyzed to generate a better conclusion referring those changes. Further experiments are to determine the identity of that species.

Time resolved resonance Raman could be performed on these samples to obtain structural information on this time regime. If it were possible to determine the profile of the evolution of the v₄ marker as a function of time it would provide excellent information on the dynamics of the system.

References

1. Kraus, D. W., and Wittenberg, J.B. **1990**. "Hemoglobin of *Lucina pectinata* / bacteria symbiosos II." *J. Biol. Chem.* 265. 16054-16059
2. Rizzi, M., Wittenberg, J.B., Coda, A., Fasano, M., Ascenzi, P., and Bolognesi, M., . **1996** "Structural Bases for sulfide recognition in *Lucina pectinata* I." *J. Mol. Biol.* 24., 86-99..
3. Antommattei-Pérez, F.M., Rosado-Ruiz, T., Cadilla, C.L., and López-Garriga, J. **1999**. "The cDNA-derived amino acid sequence of Hemoglobin I from *Lucina pectinata*." *J. Protein Chem.* 18, 831-836.
4. Cerda, J., Echevarría, Y., Morales, E., and López-Garriga, J. **1999**. "Resonance Raman Studies of the Heme-Ligand Active Site from *Lucina pectinata*." *Biospectroscopy* 5, 289-301.
5. La Mar, G.N., Nguyen, B.D., Xuefeng, Z., and Krishnamurthi, V. **1998** "Solution and Crystal structure of a Sperm Whale Myoglobin Tripke-Mutant that mimics the Sulfide Binding Hemoglobin from *Lucina pectinata*." *J. Biol. Chem.* 273, 9517-9526.
6. Silfa,, E., Almeida, M., Cerda, J., Wu, S., and López Garriga, J., **1998**. "Orientation of teh Heme Vinyl Groups in the H₂S-Binding Hbl from *Lucina pectinata*." *Biospectroscopy* 4, 311-326.
7. Cerda-Colón, J.F., Silfa, E., and Lopéz-Garriga, J. (1998). "unusual Rocking Freedom of the Heme in the Hydrogen Sulfite-Binding Hemoglobin I from *Lucina pectinta*." *J. Am. Chem. Soc.* 120, 9312-9317.

8. Pietri, R., León, R.G., Kiger, L., Marden, M., Granell, L.B., Cadilla, C.L., and López-Garriga, J.. (2005) "Tyrosine B10 and heme-ligand interactions of *Lucina pectinata* hemoglobin II: control of here reactivity." *J. Biochimica et Biophysica Acta*, 1747, 195-203.
9. León, R.G., Munier-Lehmann, H., Barzu, O., Baudin-Creusa, V., Pietri, R., López-Garriga, J., and Cadilla, C.L.. **2004** "High Level production of recombinant wild type and mutant sulfide-reactive hemoglobin I from *Lucina pectinata*." *Protein Expr. Purif.*, 38, 184-195
10. Petrich J. W., Poyart C., and Martin J. L. **1988** "*Photophysics and reactivity of heme proteins: a femtosecond absorption study of hemoglobin, myoglobin and protoheme.*" *Biochemistry* 27, 4049-4060.
11. Petrich J. W. and Martin J. L., **1989** "*Geminate recombination of diatomic ligands CO, O₂ and NO with myoglobin.*" *Chem. Phys.* 131, 31-47.
12. Martin J. L., Petrich J. W., Lambry J. C., Kuczera K., Karplus M., Poyart C. **1991** "Nitric oxide recombinant to double mutant of myoglobin: Role of ligand diffusion in a fluctuating heme pocket." *Biochemistry* 30, 3975-3987.
13. Greene B. I., Hochstrasser R. M., Weisman R. B., and Eaton W. A.**1978** "*Spectroscopy studies of oxy and carbonmonoxyhemoglobin after pulsed optical excitation.*" *Proc. Natl. Acad. Sci.* 75, (1978) 5255-5259.
14. Chernoff D. A., Hochstrasser R. M., and Steele A. W. **1980** "Geminate recombination of O₂ and hemoglobin." *Proc. Natl. Acad. Sci.* 77, 10.

15. Kholodenko Y., Gooding E. A., Dou Y., Ikeda-Saito M. and R. Hochstrasser M. **1999** “*Heme protein dynamics revealed by geminate nitric oxide recombination in mutant of iron and cobalt myoglobin.*” **Biochemistry** 38, (1999) 5918-5924.
16. Navarro A. M., Maldonado M., González-Lagoa J, López-Mejías R, López-Garriga J., Colón J. L. **1996** “*Control of Co binding states and dynamics in Hbl of Lucina pectinata by aromatic residues.*” **Inorg. Chim. Acta** 243, 161-166.
17. Das K., Beffi A., Chiancone E., and Rousseaus D. L., **1999** “*Hydroxide rather than histidine is coordinated to the heme in five-coordinate ferric Scapharca inaequivalvis hemoglobin.*” **J. Biol. Chem.** 274, 2916-2919.
18. Feis A., Marzocchi M. P., Paoli M., and Smulevich G. **1994** “*Spin State and axial ligand bonding in the hydroxide complexes of metmyoglobin, methemoglobin and horseradish peroxidase at room and low temperatures.*” **Biochemistry** 33, 4577-4583.
19. Kraus, D. W., and Wittenberg, J.B. **1990**. “*Hemoglobin of Lucina pectinata / bacteria symbiosos I.*”, **J. Biol. Chem.** 265. 16043-16053.
20. Press William H, et al. “Numerical Recepies in C. The art of scientific Computing” Second Edition. Cambridge University Press. 1999
21. Klein Daniel J. Moore Peter B, and Steitz Thomas A. **2004** “The contribution of metal ions to the structural stability of the large ribosomal subunit.” **RNA** 10 1366-1379
22. Pietri R, Lewis A., Leon R., Casabona G., Kiger L., Yeh S., Fernandez-Alberti S., Marden M., Cadilla C., and Lopez-Garriga J.. **2009** “*Factors controlling the reactivity of hydrogen sulfite with heme proteins.*” Biochemistry. 48, 4881-4894.

23. Zhu Y., Eiteman M., and Lee S., **2010**. “Conversion of glycerol to pyruvate by *e. coli* using acetate and acetate/glucose-limited fed batch process.” *J. Ind Microbiol Biotechnol*, 37, 307-312,
24. Negrerie M., Cianetti S., Vos M., Martin J-L., and Kruglik S.. **2006** “*Ultrafast heme dynamics in ferrous versus ferric cytochrome c studied by time-resolved resonance raman and transient absorption spectroscopy.*” *J. Phys Chem. B*, 110, 12766-12781.
25. Vos Marten H. **2008** “*Ultrafast dynamics of ligands within heme proteins.*” *Biochimica et Biophysical Acta*, 1777, 15-31.
26. Cao W., Christian J.F., Champion P.M., Rosca F., and Sage T.. **2001**. “*Water penetration and binding to ferric myoglobin.*” *Biochemistry*, 40, 5728-5737.
27. Ramos C.A., Pietri R., Lorenzo W., Roman E., Granell L., Cadilla C. and Lopez-Garriga J.. **2010**. “*Recombinant Hemoglobin II From Lucina pectinata: A Large-Scale Method For Hemeprotein Expression in E. coli.*” *Protein J.* 29(2): 143–151.
28. Ye, X., Demidov, A., Rosca, F., Wang, W., Kumar, A., Ionascu, D., Zhu, L., Barrick, D., Wharton, D. and Champion, P. M. **2003**. “*Investigations of heme proteins absorption line shapes, vibrational relaxation, and resonance Raman scattering on ultrafast time scales.*” *J. Phys. Chem. A*. 107, 8156-8165